scientific reports

Check for updates

OPEN

Spin–orbit coupling driven electronic phase transition and multifunctional response in lead-free K_2WCl_6 double perovskite for spintronic and energy applications

M. Abdelgaber[1,2]✉, Elkenany Brens Elkenany[3], K. Bouferrache[4,5], M. A. Ghebouli[4,6], M. Fatmi[4], Murat Yaylacı[7,8,9], Aseel Smerat[10], R. Dhahri[3] & A. M. Abdelghany[11,12]

A comprehensive first-principles study reveals a spin–orbit coupling (SOC)-driven electronic phase transition in the lead-free double perovskite K_2WCl_6. The material exhibits a robust non-relativistic half-metallic ferromagnetic state. The inclusion of SOC strongly reconstructs the electronic states near the Fermi level: GGA + U+SOC predicts a magnetic-semiconducting state with a global band gap of approximately 1.572 eV, whereas TB-mBJ + SOC yields a metallic state. This method-dependent relativistic response reflects a close competition among exchange splitting, on-site electronic correlation, and SOC in the W-5d manifold. This transition arises from strong relativistic effects associated with W 5d orbitals, enabling tunable electronic behavior relevant for spintronic applications. In addition to its electronic versatility, K_2WCl_6 demonstrates excellent mechanical and dynamical stability. The compound also exhibits significant spin-dependent optical and thermoelectric responses, including high ultraviolet absorption, spin-dependent dielectric behavior, and notable spin-resolved Seebeck coefficients. The estimated thermoelectric figure of merit increases with temperature and can be substantially enhanced through chemical-potential optimization, although the reported values remain dependent on the constant-relaxation-time and Slack-model approximations. These combined features highlight K_2WCl_6 as a promising multifunctional material for spin-dependent thermoelectric, spintronic, and optoelectronic applications, while experimental validation and more advanced many-body and scattering calculations remain necessary.

Keywords K_2WCl_6, Half-metal, Spintronics, GGA + U, Spin-orbit coupling, Thermoelectric, Phonon, Optical properties, Magnetic properties

Perovskite and double perovskite oxides and halides have attracted enormous scientific interest over the past two decades owing to their remarkable versatility and the wide range of functional properties they can exhibit. The general double perovskite formula $A_2BB'X_6$ accommodates a rich chemical diversity: the A-site can host monovalent alkali metals, the B and B' sites can accommodate transition metals with distinct valence states, and the X anion can be an oxide, fluoride, chloride, or bromide[1,2]. This compositional flexibility translates into a

[1]Department of Mathematics, College of Science and Arts, Najran University, Najran, Saudi Arabia. [2]Science and Engineering Research Center, Najran University, Najran, Saudi Arabia. [3]Department of Physics, College of Science and Arts, Najran University, Najran, Saudi Arabia. [4]Research Unit on Emerging Materials (RUEM), University Ferhat Abbas of Setif 1, Setif 19000, Algeria. [5]Department of Physics, Faculty of Sciences, University of M'sila University, Pole, Road Bourdj Bou Arreiridj, 28000 M'sila, Algeria. [6]Department of Chemistry, Faculty of Sciences, University of M'sila University, Pole, Road Bourdj Bou Arreiridj, 28000 M'sila, Algeria. [7]Department of Civil Engineering, Recep Tayyip Erdogan University, Rize 53100, Türkiye, Turkey. [8]Turgut Kıran Maritime Faculty, Recep Tayyip Erdogan University, Rize 53900, Türkiye, Turkey. [9]Dijitalpark Teknokent, Murat Yaylacı-Luzeri R&D Engineering Company, Rize 53100, Türkiye, Turkey. [10]Hourani Center for Applied Scientific Research, Al-Ahliyya Amman University, Amman 19328, Jordan. [11]Spectroscopy Department, Physics Research Institute, National Research Center, 33 Elbehouth St., Dokki 12311, Cairo, Egypt. [12]Department of General and Basic Dental Sciences, Faculty of Dentistry, Horus University, International Coastal Road, New Damietta, Damietta, Egypt. ✉email: maebrahem@nu.edu.sa

broad landscape of physical behaviors, ranging from ferromagnetism and half-metallicity to superconductivity, multiferroicity, and strong spin-orbit coupling effects[3,4]. Among the halide-based double perovskites, chloride systems of the type A_2MX_6 (M = transition metal, X = Cl) have gained renewed attention in the context of lead-free photovoltaics and spintronic device design. The replacement of toxic lead-based perovskites with environmentally benign alternatives while preserving desirable electronic properties is a central challenge of contemporary materials research[5,6]. Tungsten-based halides are particularly attractive in this regard: the d^2 electronic configuration of W^{4+} favors partially filled t_2g bands that are susceptible to strong exchange splitting, and the large spin-orbit coupling of W ($\lambda \sim 2000\ cm^{-1}$) can induce qualitative changes in the electronic topology[7,8]. K_2WCl_6 belongs to the antifluorite-derived structure family and crystallizes in Fm-3 m. In this structure, isolated WCl_6^{2-} octahedra are surrounded by eight K^+ cations in a face-centered cubic arrangement. The compound is isostructural with several well-studied members of the A_2MX_6 family, including K_2PtCl_6, K_2ReCl_6, and K_2OsCl_6[9,10]. Despite the relative simplicity of its crystal structure, K_2WCl_6 potentially harbors complex physics arising from the interplay of Coulomb correlations on the W 5 d shell, crystal-field splitting of the WCl_6 octahedron, and spin-orbit coupling[11,12]. From a theoretical standpoint, (DFT) within (GGA) often underestimates correlation effects in transition metal compounds, leading to incorrect ground states. The GGA + U method, which supplements the DFT exchange-correlation functional with an on-site Hubbard U correction on the d manifold, has proven highly effective in correcting this deficiency[13,14]. Moreover, for heavy elements such as tungsten, the inclusion of spin-orbit coupling as a relativistic correction is indispensable for accurate band structure and optical property calculations[15,16]. Several experimental and theoretical studies have been devoted to related A_2MX_6 compounds. Navas et al[17]. investigated the structural and optical properties of K_2SnCl_6 and related tin halides. Filip et al[18]. explored the electronic structure of vacancy-ordered double perovskites using hybrid functionals. Baranowski and Plochocka[19]reviewed exciton physics in metal halide perovskites. Saini et al[20]. performed first-principles calculations on K_2OsX_6 (X = Cl, Br) and reported half-metallic behavior. More recently, Ahmad et al[21]. studied the optoelectronic properties of K_2WBr_6 using DFT + U, while Hussain et al[22]. investigated K_2MoCl_6 and found similar half-metallic character. Recent comparative investigations of K_2MX_6 (M = Re, W, Ru, Os; X = Cl or Br) have further demonstrated strongly composition-dependent half-metallic, semiconducting, and optical behavior[23,24]. K_2OsCl_6 provides a relevant benchmark, combining a magnetic moment of approximately 1.99 μB, a minority-spin gap of approximately 0.8 eV, strong ultraviolet absorption, and a Seebeck coefficient of approximately 180 $\mu V\ K^{-1}$ at 900 K[25], whereas Cs_2WCl_6 exhibits pressure-tunable NIR-II emission[26]. By contrast, Sn-based chloride double perovskites mainly display semiconducting optoelectronic and thermoelectric responses[27,28]. Nonetheless, a systematic and complete first-principles investigation of K_2WCl_6 encompassing elastic, electronic, magnetic, optical, thermoelectric, phonon, and thermodynamic properties within a unified computational framework is still lacking in the literature. Accordingly, the novelty of the present study lies in demonstrating that SOC strongly reconstructs the near-Fermi electronic states of K_2WCl_6. GGA + U+SOC predicts a magnetic-semiconducting state, whereas TB-mBJ + SOC yields a metallic solution, revealing a method-dependent competition among exchange splitting, Coulomb correlation, and relativistic SOC. Recent first-principles investigations have further demonstrated the potential of chemically diverse magnetic materials for combined spintronic, optoelectronic, and thermoelectric applications. Total-energy comparisons among competing magnetic configurations have been employed to establish the magnetic stability and antiferromagnetic ordering of $CaCr_2Sb_2$, while Co_2YGe (Y = Mn, Fe) full-Heusler alloys have been investigated in terms of half-metallic ferromagnetism, exchange interactions, mechanical stability, and thermal behavior[29,30]. The modified Becke–Johnson potential has also been applied to SnX_2O_4 (X = Mg, Zn) spinels to improve the description of their electronic band gaps and optical responses[31]. Moreover, combined structural, mechanical, electronic, and thermoelectric analyses have been reported for $MgSc_2Te_4$ and MgY_2Te_4 spinels[32]. Multifunctional half-metallic, magneto-optical, and thermoelectric behavior has recently been predicted for $EuZn_2X_2$ (X = P, As), $RELi_2X_2$ (RE = Ce, Pr; X = P, As), and UCu_2P_2/UCu_2As_2 Zintl compounds[33–36]. These investigations provide a broader scientific context for evaluating the coupled magnetic, electronic, optical, mechanical, and transport properties of K_2WCl_6, while its lead-free halide composition and strong W-5d spin-orbit coupling distinguish it from Heusler, spinel, and Zintl material families.

Computational method

First-principles calculations were performed within density functional theory using the full-potential linearized augmented plane-wave (FP-LAPW) method implemented in WIEN2k 21.1[36]. In this all-electron scheme, wave functions are expanded in atomic-like functions inside non-overlapping muffin-tin (MT) spheres and in plane waves in the interstitial region, without shape approximations to the potential or charge density[37,38]. Exchange-correlation effects were treated using the PBE form of the generalized gradient approximation[39]. Correlation within the W-5d shell was included through GGA + U using the Liechtenstein formulation with the around-mean-field double-counting correction[40]. The reference calculations used U = 6.0 eV and J = 0.7 eV, consistent with related W compounds[21,22], while U = 4, 5, 6, 7, and 8 eV was additionally tested at fixed J = 0.7 eV to assess the robustness of the electronic and magnetic states. Spin-orbit coupling (SOC) was introduced in a second-variational step, giving the GGA + U+SOC description[41,42]. Spin-polarized Tran-Blaha modified Becke-Johnson calculations were also carried out with and without SOC as an independent benchmark. The MT radii were 2.50, 2.00, and 2.15 bohr for K, W, and Cl, respectively. Brillouin-zone integrations used a Γ-centered 10 × 10 × 10 Monkhorst-Pack grid for self-consistency[43] and a 16 × 16 × 16 mesh for the density of states and optical spectra. Convergence thresholds were 10^{-5} Ry in energy and 10^{-4} e in charge. Numerical stability was checked for k-point meshes from 6 × 6 × 6 to 14 × 14 × 14, RMT×Kmax = 7–9, and Gmax = 12–16 $bohr^{-1}$. The total energies at RMT×Kmax = 7, 8, and 9 were − 40279.67502510, − 40279.69279350, and − 40279.69629716 Ry, corresponding to deviations of 289.421120 and 47.669723 meV per formula unit for the two smaller bases relative to RMT×Kmax = 9. For Gmax = 12, 14, and 16 $bohr^{-1}$, the energies were − 40279.69629230, − 40279.69629712,

and − 40279.69628140 Ry; the deviation at Gmax = 12 was only 0.148302 meV per formula unit, below the 1 meV criterion. Therefore, 10 × 10 × 10, RMT×Kmax = 9, and Gmax = 12 bohr^{-1} were adopted. The magnetic moment remained 2.00001 μB throughout these tests. Structural optimization was obtained by fitting the energy-volume data to the Murnaghan equation of state[44], from which the equilibrium lattice parameter, bulk modulus, and pressure derivative were extracted. The cubic elastic constants C_{11}, C_{12}, and C_{44} were determined from small symmetry-adapted strains using the stress-strain procedure available through the WIEN2k/ELK interface[45,46], and mechanical stability was assessed using the Born criteria[47,48]. Optical properties were calculated within the random-phase approximation using the WIEN2k OPTIC module[49,50]. The imaginary dielectric function $\varepsilon_2(\omega)$ was evaluated from interband momentum matrix elements, $\varepsilon_1(\omega)$ was recovered through the Kramers-Kronig relation, and the resulting complex dielectric function was used to obtain $n(\omega)$, $k(\omega)$, $\alpha(\omega)$, $R(\omega)$, and the energy-loss function $L(\omega)$[51]. Thermoelectric transport was evaluated with BoltzTraP within the semiclassical Boltzmann equation and constant-relaxation-time approximation[52]. The GGA + U+SOC bands were used to calculate the Seebeck coefficient S, electrical conductivity σ/τ, and electronic thermal conductivity κ_e/τ as functions of carrier energy at 300, 600, and 900 K. A relaxation time $\tau = 1 \times 10^{-14}$ s was assumed to estimate absolute conductivities. The lattice thermal conductivity κl was estimated with the Slack model using temperature-dependent volumes and Debye temperatures from the GIBBS quasi-harmonic Debye analysis, while the Grüneisen parameter was obtained from the Slater approximation. The overall thermoelectric performance was estimated from $ZT = S^2\sigma T/(\kappa_e + \kappa l)$. Lattice dynamics were investigated using the finite-displacement method through PHONON and PHONOPY interfaced with WIEN2k[53–56].

Results and discussion

K_2WCl_6 crystallizes in the cubic Fm-3 m (No. 225) space group, which is the antifluorite-type structure adopted by most A_2MX_6 compounds[9]. In this structure, W atoms occupy the 4a Wyckoff position (0, 0, 0), K atoms sit at 8c (0.75, 0.25, 0.25), and Cl atoms are located at 24e (0.50, 0, 0.2579), forming regular WCl_6 octahedra that are well-separated by K^+ cations. The total energy was calculated as a function of volume over a range of ± 10% around the experimental value and fitted to the Murnaghan equation of state[44]. Figure 1 shows the energy-volume (E-V) curve for K_2WCl_6, which displays the characteristic parabolic shape expected for a mechanically stable compound. The minimum of the curve defines the equilibrium volume from which the optimized lattice parameter and bulk modulus are extracted. The results are summarized in Table 1.

The calculated lattice constant $a_0 = 9.84$ Å agrees very well with the experimental single-crystal X-ray diffraction value of 9.822 Å reported for cubic K_2WCl_6 at 293 K 57[44], as well as with theoretical results for related isostructural compounds[9,10,22]. The deviation between the calculated and experimental values is only approximately 0.18%, confirming the reliability of the present structural optimization. The experimental study also confirms the cubic Fm-3m (No. 225) structure, with a unit-cell volume of 947.6 Å^3 and Z = 4[57]. The B = 48.06 GPa with B' = 4.48 indicates moderate compressibility, consistent with the open halide framework. These structural parameters serve as the starting point for all subsequent property calculations.

The three independent elastic constants C_{11}, C_{12}, and C_{44} of cubic K_2WCl_6 were computed using the stress-strain method and are presented in Table 2 together with the derived mechanical moduli, acoustic wave velocities,

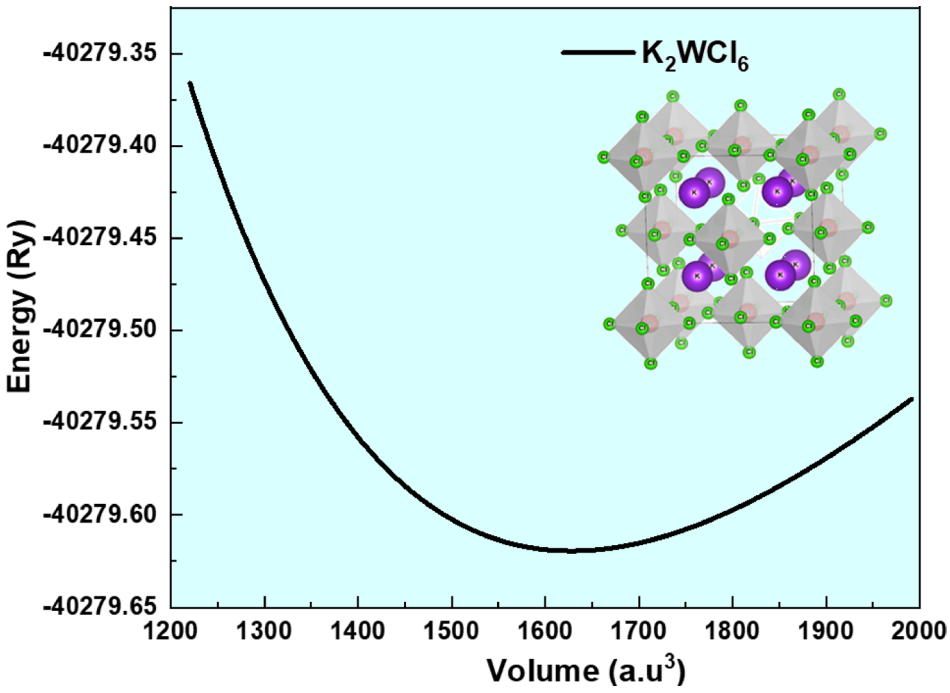


Fig. 1. Calculated total energy versus unit cell volume for K_2WCl_6.

Compound	Space group	a (Å)	bulk modulus	B'	Atom	Wyckoff	x	Y	z
K_2WCl_6	Fm-3 m (225)	9.84	48.06	4.48	W	4a	0	0	0
					K	8c	0.75	0.25	0.25
					Cl	24e	0.50	0	0.2579

Table 1. Calculated structural parameters and atomic positions of the K_2WCl_6 compound.

Property	Voigt	Reuss	Hill
Elastic Constants	C_{11} = 95.867 GPa	C_{12} = 24.177 GPa	C_{44} = 17.285 GPa
Bulk modulus B (GPa)	48.074	48.074	48.074
Shear modulus G (GPa)	24.709	21.800	23.255
Young's modulus E (GPa)	63.285	56.813	60.077
Poisson's ratio ν	0.281	0.303	0.292
Transverse wave velocity (m/s)	2666.746		
Longitudinal wave velocity (m/s)	4917.668		
Average wave velocity (m/s)	2975.592		
Debye temperature θD (K)	296.079		

Table 2. Elastic constants, mechanical properties, acoustic wave velocities, and Debye temperature of K_2WCl_6.

Method	Majority-spin/electronic behavior	Minority-spin/global gap (eV)	M_{tot} (μB/f.u.)	Calculated state
GGA + U, (U = 6) eV	Metallic spin-up channel	4.279 (spin-down)	2.00001	Half-metallic FM
TB-mBJ	Metallic spin-up channel	3.053 (spin-down)	2.00	Half-metallic FM
GGA + U+SOC	Global semiconducting gap	1.572	1.90822	Magnetic semiconductor
TB-mBJ + SOC	Bands cross (EF)	0	1.93730	Metallic FM

Table 3. Comparison of the electronic and magnetic properties obtained using the different approximations.

and Debye temperature. The mechanical stability of a cubic crystal requires satisfaction of the Born criteria: $C_{11} > 0$, $C_{44} > 0$, $C_{11} - C_{12} > 0$, and $C_{11} + 2\,C_{12} > 0$[47]. All four conditions are fulfilled (C_{11} = 95.867 GPa, C_{12} = 24.177 GPa, C_{44} = 17.285 GPa), confirming that the compound is mechanically stable. The bulk modulus derived from the Voigt-Reuss-Hill (VRH) averages (BH = 48.074 GPa) is in excellent agreement with the equation-of-state value, providing an internal consistency check. The shear modulus GH = 23.255 GPa and Young's modulus EH = 60.077 GPa reflect the moderate rigidity of the halide framework. The Poisson's ratio νH = 0.292 is close to 0.30, which is characteristic of central-force solids and suggests predominantly ionic bonding with a non-negligible covalent contribution from the W–Cl bonds[58]. The Pugh ratio B/G = 2.07 exceeds the critical value of 1.75, classifying K_2WCl_6 as a ductile material[59]. The Debye temperature calculated from the average sound velocity (θD = 296.079 K) provides a useful measure of the characteristic phonon frequency scale. This relatively modest value reflects the heavy atomic masses of W and Cl and the soft nature of the W–Cl bond, and it is consistent with the phonon density of states discussed in Sect. 3.6. The transverse, longitudinal, and average acoustic velocities are 2666.746, 4917.668, and 2975.592 m/s, respectively, confirming the moderate acoustic stiffness of the compound.

The electronic properties of K_2WCl_6 were calculated within the GGA + U and GGA + U+SOC frameworks. The results are summarized in Table 3, and the spin-polarized band structures computed along the high-symmetry path W–L–Γ–X–K in the Brillouin zone are presented in Fig. 2. The Spin-polarized electronic band structures of K_2WCl_6 along the high-symmetry path W–L–Γ–X–K in the Brillouin zone, calculated using (a, b) GGA + U and (c, d) GGA + U+SOC for spin-up (↑) and spin-down (↓) channels. The Fermi level is set to zero. The majority-spin and minority-spin W-t2g-derived bands are explicitly identified by arrows in the non-relativistic GGA + U panels, while the relativistic panels indicate the SOC-mixed W-t2g-derived states near the Fermi level. As explicitly labeled in Fig. 2, the majority-spin W-t2g manifold forms the bands crossing the Fermi level, whereas the minority-spin W-t2g manifold is shifted toward the conduction region and defines the lower edge of the minority-spin gap. In the GGA + U+SOC panels, the labeled states should be regarded as SOC-mixed W-t2g-derived states because the relativistic eigenfunctions are no longer separable into independent pure-spin channels.

Within GGA + U, the spin-up channel of K_2WCl_6 is metallic, with bands crossing the Fermi level, while the spin-down channel opens a band gap of 3.07 eV. This coexistence of metallic behavior in one spin channel with semiconducting behavior in the other defines the half-metallic ferromagnetic (HMF) state[60,61]. Half-metals are of paramount interest for spintronics because they theoretically provide 100% spin-polarized carriers at the Fermi level, which maximizes the efficiency of spin injection and magnetoresistance in device applications[62].

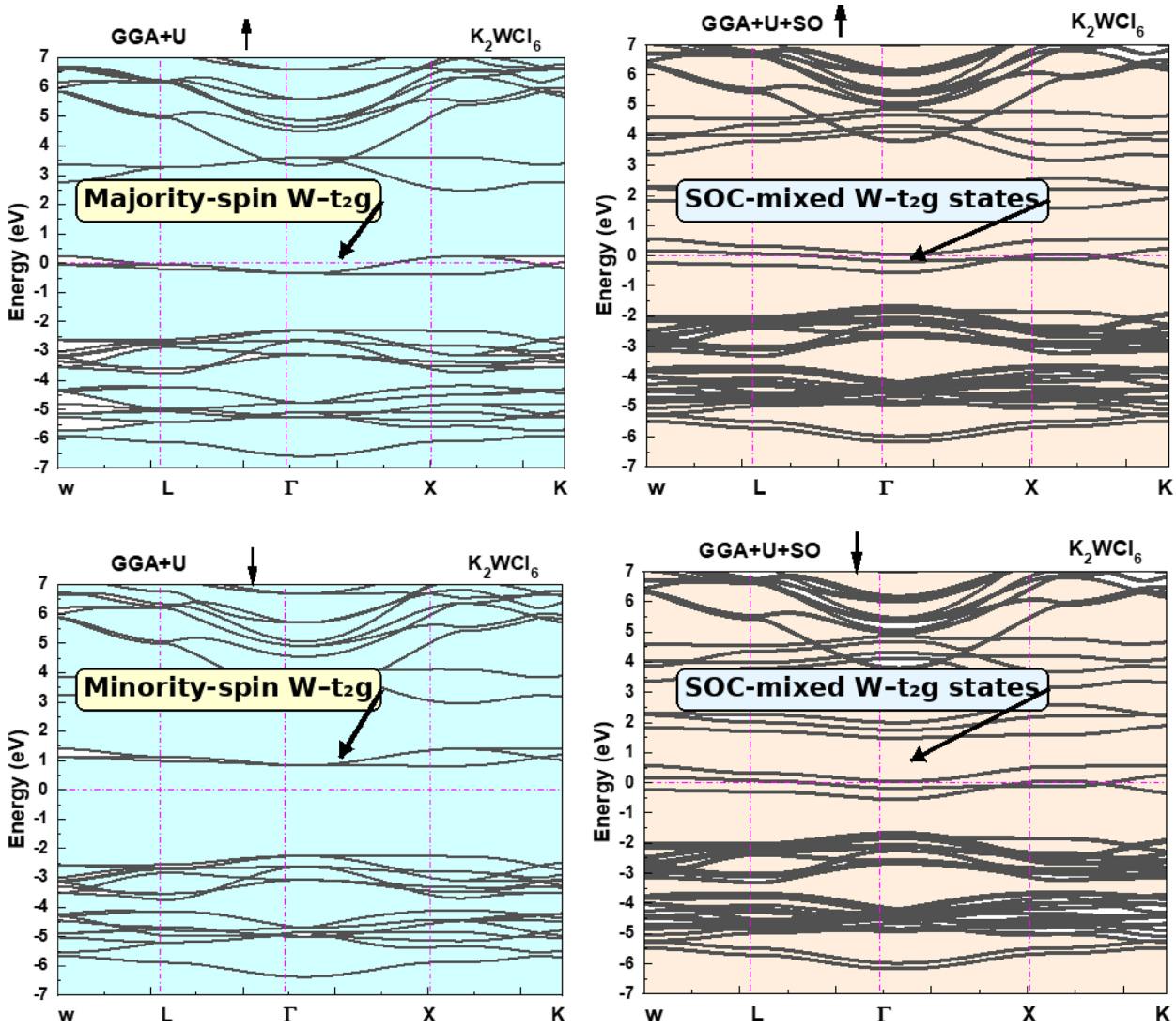


Fig. 2. Spin-polarized electronic band structures of K_2WCl_6. for spin-up (↑) and spin-down (↓) channels.

The half-metallic character of K_2WCl_6 is driven by the strong exchange splitting of the W 5 d (t_2g) manifold: the majority-spin t_2g bands are pushed below the Fermi level and hybridize with Cl 3p states, while the minority-spin t_2g bands are shifted above the Fermi level by the combined action of exchange splitting and the Hubbard U correction. As summarized in Table 3, both non-relativistic approaches predict the same qualitative half-metallic phase, whereas the inclusion of SOC leads to a method-dependent relativistic electronic state.

The orbital-resolved analysis indicates that the electronic reconstruction near the Fermi level is governed mainly by the W-t2g states rather than the higher-lying W-eg manifold. In the octahedral crystal field, the W-5d states split into lower-energy t2g and higher-energy e.g. components. The partially occupied t2g states form the band edges and the metallic majority-spin channel, whereas the e.g. states contribute predominantly at higher conduction-band energies. The Cl-3p states hybridize strongly with the W-t2g manifold and therefore participate indirectly in the SOC-induced redistribution of the near-Fermi electronic states. To determine whether this result depends on the selected Hubbard parameter, systematic calculations were performed for U = 4, 5, 6, 7, and 8 eV, with J = 0.7 eV fixed. All five calculations converged to the same qualitative half-metallic state. The majority-spin channel remained metallic throughout the examined range, whereas the minority-spin gap increased systematically from 3.822 eV at U = 4 eV to 4.048, 4.279, 4.504, and 4.750 eV for U = 5, 6, 7, and 8 eV, respectively. The total magnetic moment remained essentially unchanged at 2.00001 μB per formula unit for all examined values of U. By contrast, the local W moment increased gradually from 1.58877 μB at U = 4 eV to 1.76237 μB at U = 8 eV. The preservation of the metallic majority-spin channel, finite minority-spin gap, and integer total magnetic moment over the entire U = 4–8 eV interval demonstrates that the predicted non-relativistic half-metallicity is robust and is not an artifact of choosing U = 6 eV. The corresponding evolution of the minority-spin gap and magnetic moments is summarized in Table 4.

To identify the most stable magnetic configuration, independent self-consistent calculations were performed for the non-magnetic (NM), ferromagnetic (FM), and a representative antiferromagnetic (AFM) state. For each

U (eV)	Spin-up character	Spin-down gap (eV)	M_{tot} (μB)	M_W (μB)	Calculated state
4	Metallic	3.822	2.00001	1.58877	Half-metallic FM
5	Metallic	4.048	2.00001	1.63188	Half-metallic FM
6	Metallic	4.279	2.00001	1.67465	Half-metallic FM
7	Metallic	4.504	2.00001	1.71203	Half-metallic FM
8	Metallic	4.750	2.00001	1.76237	Half-metallic FM

Table 4. Dependence of the calculated electronic and magnetic properties of K_2WCl_6 on the Hubbard parameter, with J = 0.7 eV.

Magnetic configuration	Equilibrium energy (Ry/f.u.)	ΔE relative to FM (meV/f.u.)	Relative stability
FM	−40279.681414	0	Lowest-energy configuration
AFM	−40279.676017	73.43	Metastable
NM	−40279.648743	444.52	Less stable

Table 5. Relative stability of the investigated magnetic configurations of K_2WCl_6.

T (K)	κ_l (W m^{-1} K^{-1})	ZT at (E_F)	ZT_{max}	Optimal (u-E_F) (eV)	PF_{max} (W m^{-1} K^{-2}) × 10^{-3}
300	2.363	0.016	0.367	−1.129	5.1
600	1.034	0.083	1.961	−1.216	9.31
900	0.598	0.241	3.713	+0.353	1.084

Table 6. Estimated thermoelectric parameters of K_2WCl_6 at the intrinsic Fermi level and at the optimal chemical potential.

configuration, the total energy was calculated as a function of volume and fitted using the same equation-of-state procedure. The equilibrium energy extracted from each fit was adopted as the stability criterion, with the configuration exhibiting the lowest equilibrium total energy identified as the magnetic ground state among the investigated collinear arrangements. To further examine the stability of the magnetic solution against competing collinear configurations, the total energies of the non-magnetic (NM), ferromagnetic (FM), and a representative antiferromagnetic (AFM) state were compared using equation-of-state fits. The equilibrium energies per formula unit were −40279.681414, −40279.676017 and −40279.648743 for the FM, AFM, and NM configurations, respectively. The AFM and NM states lie approximately 73.43 and 444.52 meV per formula unit above the FM state. Therefore, among the explicitly examined collinear magnetic configurations, the FM state is energetically favored. These relative energies and the resulting stability order are summarized in Table 6.

The Spin-polarized electronic band structures of K_2WCl_6 along the high-symmetry path W–L–Γ–X–K in the Brillouin zone, calculated using (a, b) TB-mBJ and (c, d) TB-mBJ + SOC for the positive and negative spin projections. The horizontal dashed line represents the Fermi level at 0 eV. The arrows indicate the W-t2g-derived states closest to the Fermi level and illustrate their reconstruction following the inclusion of SOC. As shown in Fig. 3, TB-mBJ preserves the non-relativistic half-metallic state, with a metallic spin-up channel and a finite spin-down gap. By contrast, TB-mBJ + SOC produces bands crossing the Fermi level, demonstrating a pronounced SOC-induced reconstruction of the near-Fermi W-t2g-derived states. Because the relativistic eigenfunctions contain mixed spin components, the TB-mBJ + SOC panels should be interpreted as spin-projected representations rather than as completely independent pure-spin channels.

The electronic structure was further examined using the spin-polarized TB-mBJ potential. TB-mBJ reproduces the qualitative half-metallic character obtained with GGA + U: the spin-up channel remains metallic, while the spin-down channel exhibits a gap of 3.053 eV. Although this value is smaller than the GGA + U minority-spin gap of 4.279 eV obtained at U = 6 eV, both approximations predict the same non-relativistic electronic phase. This independent calculation therefore supports the robustness of the half-metallic ground-state description.

Taken together, the systematic U-dependence study and the independent TB-mBJ calculation show that the predicted non-relativistic half-metallic state is not an artifact of the single choice U = 6 eV. The metallic majority-spin channel and finite minority-spin gap are preserved throughout the investigated U = 4–8 eV range and are reproduced qualitatively by TB-mBJ. However, the comparison between GGA + U+SOC and TB-mBJ + SOC shows that the precise relativistic electronic phase remains sensitive to the treatment of exchange and correlation. Hybrid-functional + SOC or GW calculations would provide a more advanced quantitative benchmark, but these computationally demanding treatments were not performed in the present work. Because only one representative AFM arrangement was investigated, the present energy comparison provides only one independent FM–AFM energy difference and is therefore insufficient to determine three independent exchange parameters J_1, J_2, and J_3. A reliable Heisenberg-model mapping would require several linearly independent AFM

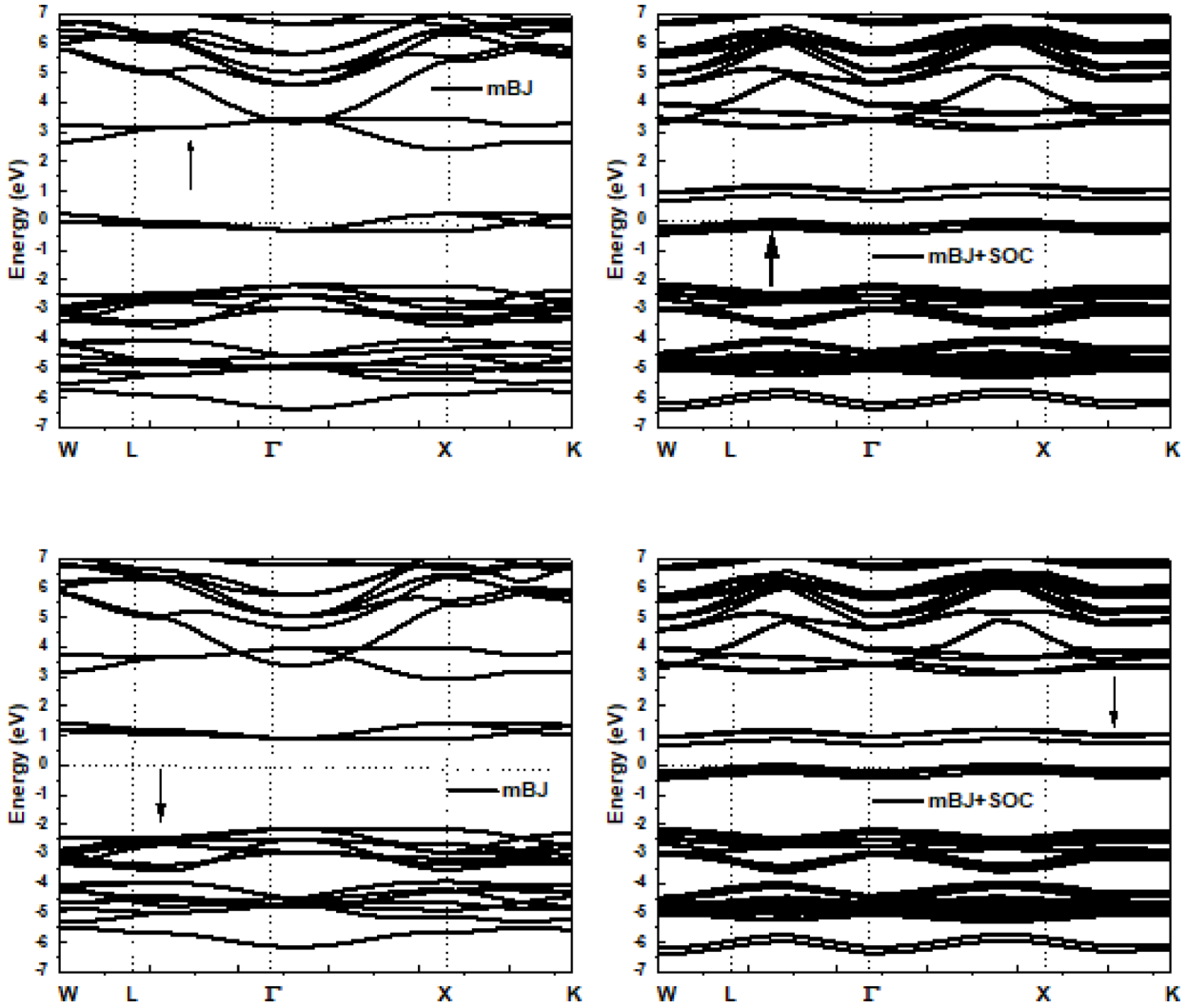


Fig. 3. Spin-polarized electronic band structures of K_2WCl_6 for the positive and negative spin projections.

configurations constructed within an appropriate magnetic supercell. Consequently, underdetermined exchange constants and a Curie temperature derived from an incomplete magnetic mapping are not reported. It should also be emphasized that the present comparison establishes only the relative energetic stability of the explicitly investigated collinear NM, FM, and representative AFM configurations. Magnetic anisotropy energies, non-collinear magnetic states, finite-temperature spin fluctuations, and the Curie temperature were not evaluated. Therefore, the present results support an FM ground state among the examined configurations, but they do not by themselves demonstrate long-range ferromagnetic stability at a specific operating temperature. A complete finite-temperature magnetic characterization would require additional independent magnetic configurations, exchange-parameter mapping, magnetic-anisotropy calculations, and statistical spin simulations. The total magnetic moment obtained without SOC is approximately 2.00 μB per formula unit, an integer value consistent with the predicted half-metallic state. The dominant magnetic contribution is associated with the W 5 d states, whereas only a small moment is induced on the Cl atoms through W-5d–Cl-3p hybridization. The inclusion of SOC within the GGA + U+SOC approach substantially reconstructs the electronic states near the Fermi level. Unlike the non-relativistic half-metallic solution, the converged GGA + U+SOC calculation produces a global band gap of approximately 1.572 eV and a total magnetic moment of 1.90822 μB per formula unit. The reduction of the magnetic moment from approximately 2.00 to 1.90822 μB reflects SOC-induced mixing of the spin components and the consequent loss of perfect integer spin polarization. According to this approximation, K_2WCl_6 is therefore classified as a magnetic semiconductor rather than a half-metal. A complementary TB-mBJ + SOC calculation produces finite electronic states at the Fermi level and consequently predicts a metallic state. The corresponding total magnetic moment is 1.93730 μB per formula unit. The comparison demonstrates that both relativistic treatments predict pronounced SOC-induced reconstruction and a reduction of the ideal integer magnetic moment, although the precise metallic or semiconducting character of the near-Fermi bands remains sensitive to the treatment of exchange and correlation. This sensitivity reflects a close competition among W-5d exchange splitting, on-site Coulomb interaction, and relativistic SOC. A direct inspection of the relativistic TB-mBJ + SOC band structure confirms that two W-5d-derived bands cross the Fermi level. Because

SOC produces spinor eigenstates containing mixed spin components, the relativistic spin-up and spin-down band-energy files are identical and should not be interpreted as two independent pure-spin band structures. This behavior provides direct evidence that SOC mixes the original majority- and minority-spin states and reconstructs the partially occupied W-t2g-derived bands nearest to EF.

A quantitative analysis of the spin-projected TB-mBJ + SOC density of states was also performed at the Fermi level. Linear interpolation gives N↑(EF) ≈ 0.6813 and N↓(EF) ≈ 0.0237 states eV − 1 per formula unit. The DOS spin polarization was evaluated using:

$$P_{\mathrm{DOS}}(\mathrm{E_F}) = \frac{\mathrm{N_\uparrow}(\mathrm{E_F}) - \mathrm{N_\downarrow}(\mathrm{E_F})}{\mathrm{N_\uparrow}(\mathrm{E_F}) + \mathrm{N_\downarrow}(\mathrm{E_F})}$$

yielding PDOS(EF) ≈ 93.3%. The W-5d contributions at the Fermi level are approximately 0.2996 and 0.0130 states eV − 1 for the positive and negative spin projections, respectively, confirming that the relativistic metallic states remain strongly dominated by W-5d orbitals. The finite minority-spin contribution demonstrates that SOC suppresses perfect 100% spin polarization, although a highly spin-polarized DOS is retained in the TB-mBJ + SOC metallic solution. The quantity PDOS(EF) characterizes the spin polarization of the density of states and should not be confused with the transport-current polarization, which additionally depends on spin-dependent carrier velocities and relaxation times. A rigorous current-polarization calculation would therefore require a spin-resolved transport treatment beyond the present DOS analysis. The total and partial densities of states shown in Figs. 4 and 5 provide further insight into the electronic structure. In the non-relativistic GGA + U calculation, the valence-band region contains strongly hybridized W 5 d and Cl 3p states. The states crossing the Fermi level in the metallic channel are predominantly derived from the partially occupied W 5 d t2 manifold. The K-derived states contribute negligibly around the Fermi energy and occur mainly in deeper valence or higher conduction-energy regions.

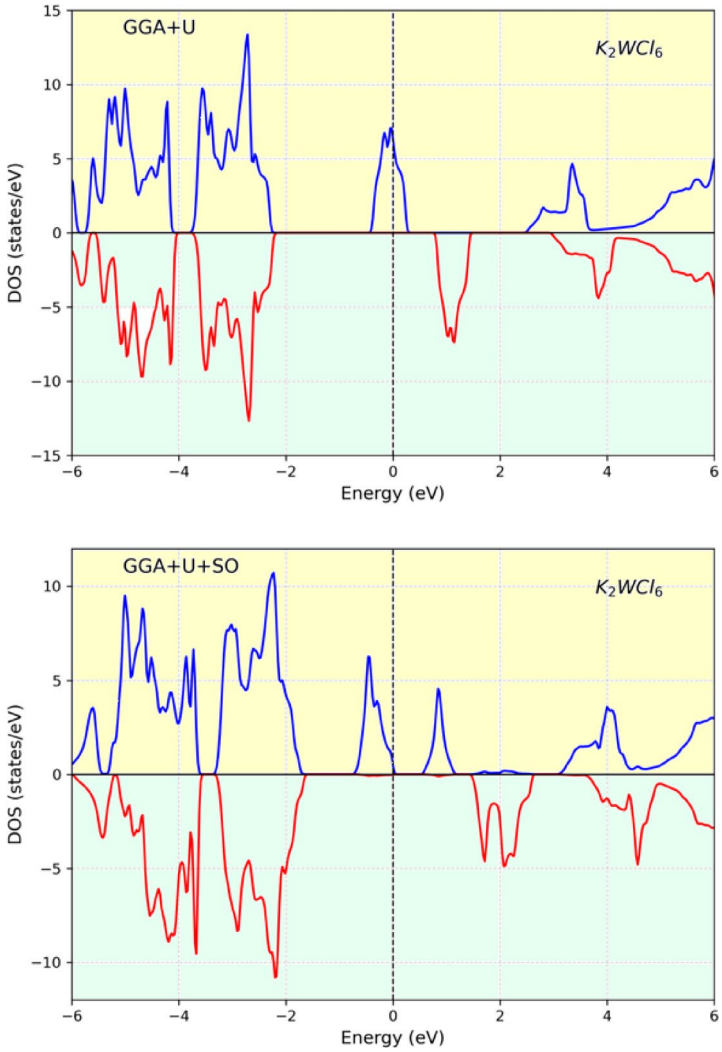


Fig. 4. Total density of states (TDOS) of K_2WCl_6 computed using GGA + U (upper) and GGA + U+SOC (lower) for both spin channels. The vertical dashed line marks the Fermi level at 0 eV.

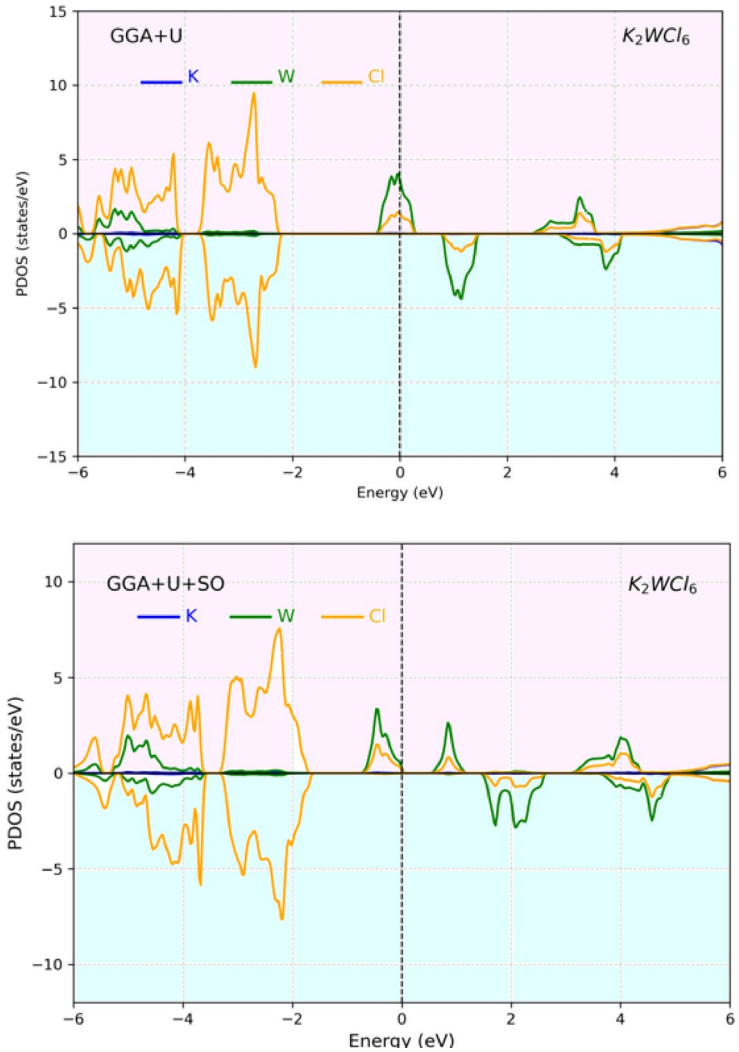


Fig. 5. Partial density of states (PDOS) of K_2WCl_6 computed using GGA + U and GGA + U+SOC, showing contributions from K, W, and Cl atoms for spin-up and spin-down channels. The Fermi level is at 0 eV.

The GGA + U+SOC atom-resolved DOS exhibits a clear depletion of electronic states around the Fermi level, consistent with the calculated global gap of approximately 1.572 eV. The upper valence-band region is principally formed by Cl-derived states hybridized with W-5d states, while the lower conduction-band edge is predominantly associated with W-derived states. K makes only a negligible contribution to both band edges. Because SOC mixes the two spin components, the positive and negative portions of the relativistic DOS should be interpreted as spin-projected contributions rather than as completely independent spin-up and spin-down channels. In contrast, the TB-mBJ + SOC electronic structure retains finite states at the Fermi level, confirming its metallic classification. Accordingly, the comparison between the GGA + U+SOC and TB-mBJ + SOC results reveals a method-dependent near-Fermi electronic phase. Hybrid-functional calculations combined with SOC or a many-body treatment could provide further clarification, but such calculations are beyond the scope of the present all-electron investigation. Because the present WIEN2k calculations employ the physical SOC interaction at its full strength, an artificial scaling study using $\lambda = 0–1$ was not performed. Consequently, a critical SOC scaling parameter and the mathematical order of the electronic transition are not assigned. The comparison between calculations without SOC and with full SOC instead establishes that the relativistic interaction causes a substantial reconstruction of the W-t2g-dominated states. The different electronic phases predicted by GGA + U+SOC and TB-mBJ + SOC further show that the detailed position of the near-Fermi bands is sensitive to the treatment of exchange and correlation. Therefore, the relativistic electronic phase should be regarded as method-dependent until it is verified by hybrid-functional + SOC, many-body calculations, or experimental spectroscopy. From a device perspective, the predicted spin-polarized electronic structure and pronounced SOC response provide only an initial indication of possible spintronic functionality. Recent experimental work on chiral antiferromagnetic devices has demonstrated that electrical manipulation of magnetic order requires an appropriate device heterostructure, efficient spin–orbit torque generation, controlled magnetic anisotropy, and sufficiently low switching-current densities[63,64]. Therefore, the present bulk calculations do not establish electrical magnetic switching in K_2WCl_6. Experimental thin-film growth, magnetic-anisotropy measurements,

interface engineering, and current-induced switching studies would be required before applications in spin valves, magnetic tunnel junctions, or spin–orbit-torque devices could be assessed.

The optical properties of K_2WCl_6 were investigated by computing the frequency-dependent complex dielectric function $\varepsilon(\omega) = \varepsilon_1(\omega) + i\varepsilon_2(\omega)$ and the derived spectra. Figure 6 shows the optical absorption coefficient $\alpha(\omega)$ for spin-up and spin-down channels. In the GGA + U case, the spin-up channel exhibits absorption onset near 0 eV consistent with its metallic character, whereas the spin-down channel shows a threshold around 3.07 eV, corresponding to the half-metallic gap. Several absorption peaks appear at higher energies (4–9 eV), attributable to interband transitions from the W 5d–Cl 3p bonding states to the antibonding and conduction band states[65]. The inclusion of SOC in GGA + U+SOC modifies the absorption profile notably: the spin-down threshold disappears, and the spectral weight redistributes over a broader energy range due to band mixing. The high absorption coefficients ($\alpha \sim 10^5$ cm^{-1}) in the UV range indicate that K_2WCl_6 can effectively absorb high-energy photons, a property relevant for UV photodetection.

The distinct absorption behavior of the two spin channels can be directly understood from their corresponding electronic structures. In the non-relativistic GGA + U description, the majority-spin channel contains partially occupied W-t2g-derived bands crossing the Fermi level. Consequently, low-energy electronic transitions are allowed and the absorption spectrum begins close to zero photon energy. In contrast, the minority-spin channel possesses a finite band gap, so photon absorption requires transitions from the occupied Cl-3p/W-t2g-hybridized valence states to the unoccupied W-5d-derived conduction states. This produces a delayed optical onset near the calculated minority-spin gap. After the inclusion of SOC, the original majority- and minority-spin states become mixed, and the independent pure-spin absorption edges are no longer strictly preserved. The SOC-induced reconstruction of the W-t2g-dominated states modifies the available initial and final states, leading to shifts, broadening, and redistribution of the absorption intensity between the spin-projected spectra. Thus, the low-energy absorption response is controlled primarily by the metallic or gapped character of the near-Fermi electronic states, whereas the intense ultraviolet absorption originates from the larger joint density of Cl-3p and W-5d states participating in higher-energy interband transitions. To provide a more detailed physical interpretation of the optical response, the main absorption features were correlated with the calculated band structures and orbital-resolved densities of states. The low-energy optical response is primarily associated with transitions from occupied Cl-3p/W-t2g hybridized states near the upper valence region toward unoccupied W-5d-derived states. The structures appearing in the intermediate-energy range of approximately 4–7 eV are mainly attributed to transitions from Cl-3p-dominated valence states to the W-t2gt and W-ege conduction manifolds. The more intense ultraviolet features above approximately 7–9 eV involve transitions from deeper Cl-3p bonding states toward higher-energy W-5d antibonding states. The changes in peak intensity and spectral position after the inclusion of SOC reflect the relativistic redistribution and mixing of the W-5d electronic states. These assignments are based on the correspondence between the energy ranges of the band structure, PDOS, and optical spectra and should therefore be regarded as qualitative orbital-level interpretations. A rigorous identification of individual band-to-band transitions and the specific k-points contributing to each optical peak would require a dedicated decomposition of the optical transition matrix elements or a k-resolved joint-density-of-states analysis. The real and imaginary parts of the dielectric function are presented in Fig. 7. The static dielectric constant $\varepsilon_1(0)$ in the spin-up channel (GGA + U) is large and positive, exceeding 20, consistent with the metallic screening. In the spin-down channel, $\varepsilon_1(0) \approx 5.8$ is more moderate and reflects the dielectric response of the semiconductor. Multiple oscillations in $\varepsilon_1(\omega)$ corresponding to resonances in $\varepsilon_2(\omega)$ are visible in the 3–10 eV range[66]. The resonant structures in $\varepsilon_1(\omega)$ are associated with the corresponding interband-transition peaks in $\varepsilon_2(\omega)$. In particular, the dielectric response in the 3–7 eV region mainly originates from transitions involving the upper Cl-3p/W-t2g hybridized valence states and the low-lying W-5d conduction states, whereas the higher-energy dielectric features are associated with transitions toward the W-ege and higher antibonding manifolds.

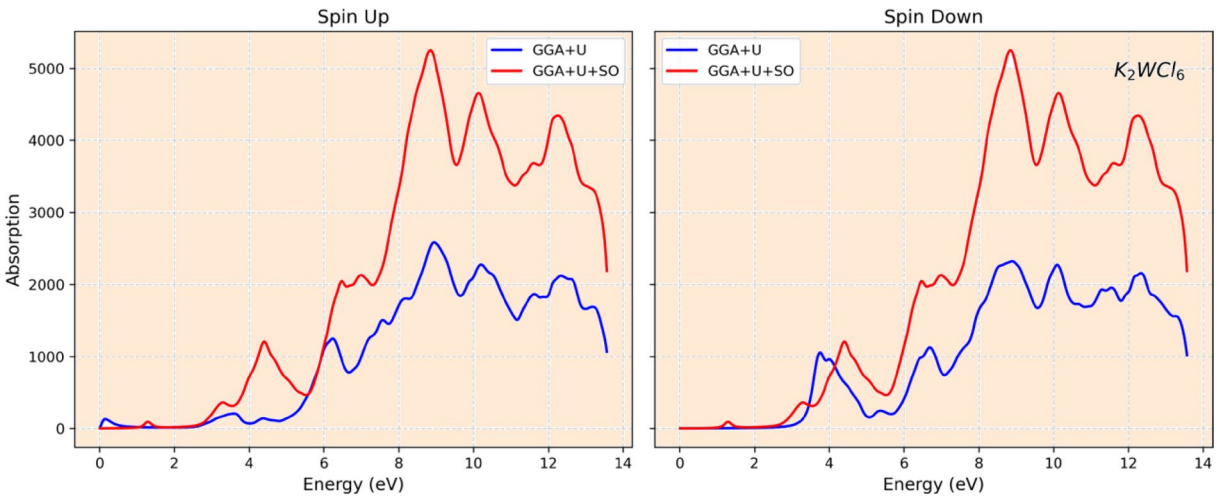


Fig. 6. Optical absorption spectra of K_2WCl_6 calculated using GGA + U and GGA + U+SOC.

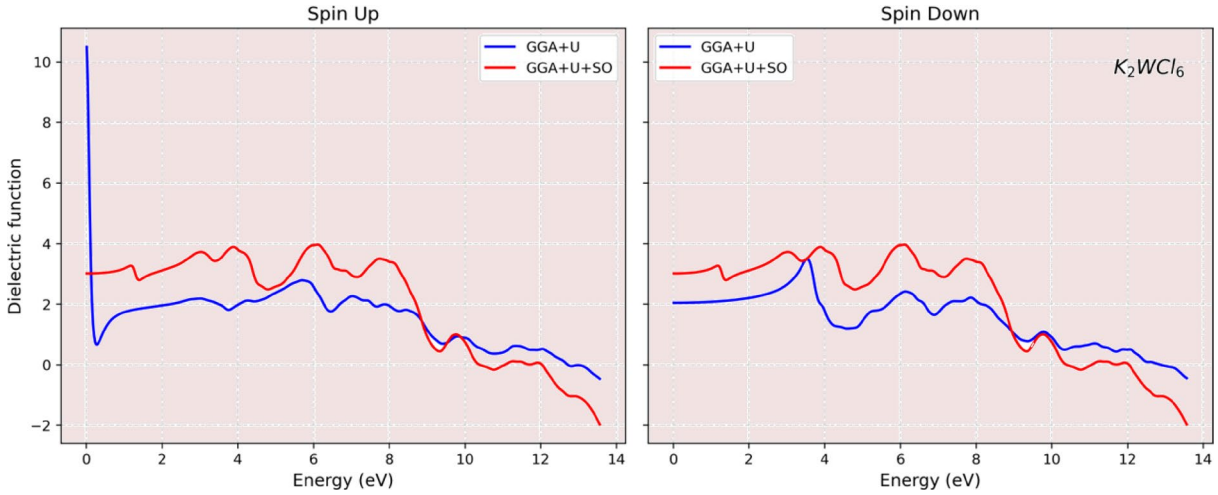


Fig. 7. Real part $\varepsilon_1(\omega)$ of the complex dielectric function of K_2WCl_6 calculated using GGA + U and GGA + U+SOC.

The SOC-induced shifts and broadening of these structures are consistent with the reconstruction of the W-5d states observed in the relativistic electronic structure.

Figure 8 presents the refractive index n(ω) and R(ω). The zero-frequency refractive index n(0) is approximately 1.9 for the spin-down channel, within the range typical of wide-gap halides. The reflectivity spectrum shows a broad plateau above 50% for energies exceeding 8 eV in both channels, indicating strong reflection in the deep UV regime. The spin-dependent differences in n(ω) and R(ω) suggest potential applications of K_2WCl_6 in spin-sensitive optical coatings and photonic devices[67,68]. More cautiously, the differences between the spin-projected optical spectra indicate a potentially spin-dependent optical response. However, this result alone does not establish a magneto-optical Kerr or Faraday effect, because these phenomena require the calculation of the off-diagonal components of the dielectric tensor. Therefore, the present results are interpreted as evidence of spin-dependent optical transitions rather than as a direct prediction of a specific magneto-optical device response.

The energy loss function $L(\omega) = -\mathrm{Im}[1/\varepsilon(\omega)]$, displayed in Fig. 9, exhibits prominent plasmon peaks around 10–12 eV for both spin channels and both computational methods. These peaks correspond to collective oscillations of the valence electron density and mark the onset of high transparency in the material[69]. The plasmon energy is slightly shifted and broadened by SOC effects, consistent with the redistribution of spectral weight observed in the dielectric function.

The calculated optical-conductivity spectrum follows the main structures of the absorptive dielectric response, confirming that the dominant conductivity features originate from interband transitions involving Cl-3p and W-5d states. The optical conductivity increases substantially in the ultraviolet region, where the strongest absorption features occur. It should be noted that the present optical calculations include interband contributions only, and no intraband or Drude contribution was added. Consequently, the low-frequency response of the metallic channel should not be interpreted as a complete description of its free-carrier optical conductivity. Furthermore, the optical properties were evaluated within the independent-particle RPA framework, which does not explicitly include electron–hole interactions. Excitonic effects and the exciton binding energy were therefore not calculated, and the predicted absorption edges should be interpreted as single-particle optical thresholds. A quantitative description of excitonic peaks would require calculations based on the Bethe–Salpeter equation or an equivalent many-body treatment. The translation of favorable optical spectra into a practical optoelectronic device additionally depends on defect passivation, carrier injection, interfacial energy alignment, film quality, and operational stability. For example, ligand coordination and defect control in $CsPbI_3$ quantum dots have enabled highly efficient pure-red light-emitting diodes by simultaneously improving their structural, optical, and electrical characteristics[70,71]. This device-level example illustrates the importance of materials and interface engineering in halide optoelectronics. Nevertheless, the present calculations for K_2WCl_6 concern bulk absorption and dielectric properties only; they do not evaluate photoluminescence quantum yield, radiative recombination, carrier injection, electroluminescence efficiency, or complete device architecture. Accordingly, UV photodetection and related optoelectronic applications should be regarded as prospective applications requiring experimental validation.

The thermoelectric performance of K_2WCl_6 was assessed through the spin-resolved Seebeck coefficient S(E), electrical conductivity per relaxation time $\sigma/\tau(E)$, and electronic thermal conductivity per relaxation time $\kappa_e/\tau(E)$ as functions of the reduced energy $(E - E_F)$ at three temperatures: 300 K, 600 K, and 900 K. All thermoelectric calculations were performed within the GGA + U+SOC framework, which All transport calculations were performed using the GGA + U+SOC electronic structure as a consistent relativistic input, using the BoltzTraP code[52]. The BoltzTraP calculations were performed within the constant relaxation time approximation (CRTA). In this approximation, the carrier relaxation time is assumed to be independent of energy, temperature, carrier concentration, and spin channel. Therefore, the calculated σ/τ and κ_e/τ quantities should be interpreted primarily as band-structure-dependent transport functions rather than absolute experimentally measurable

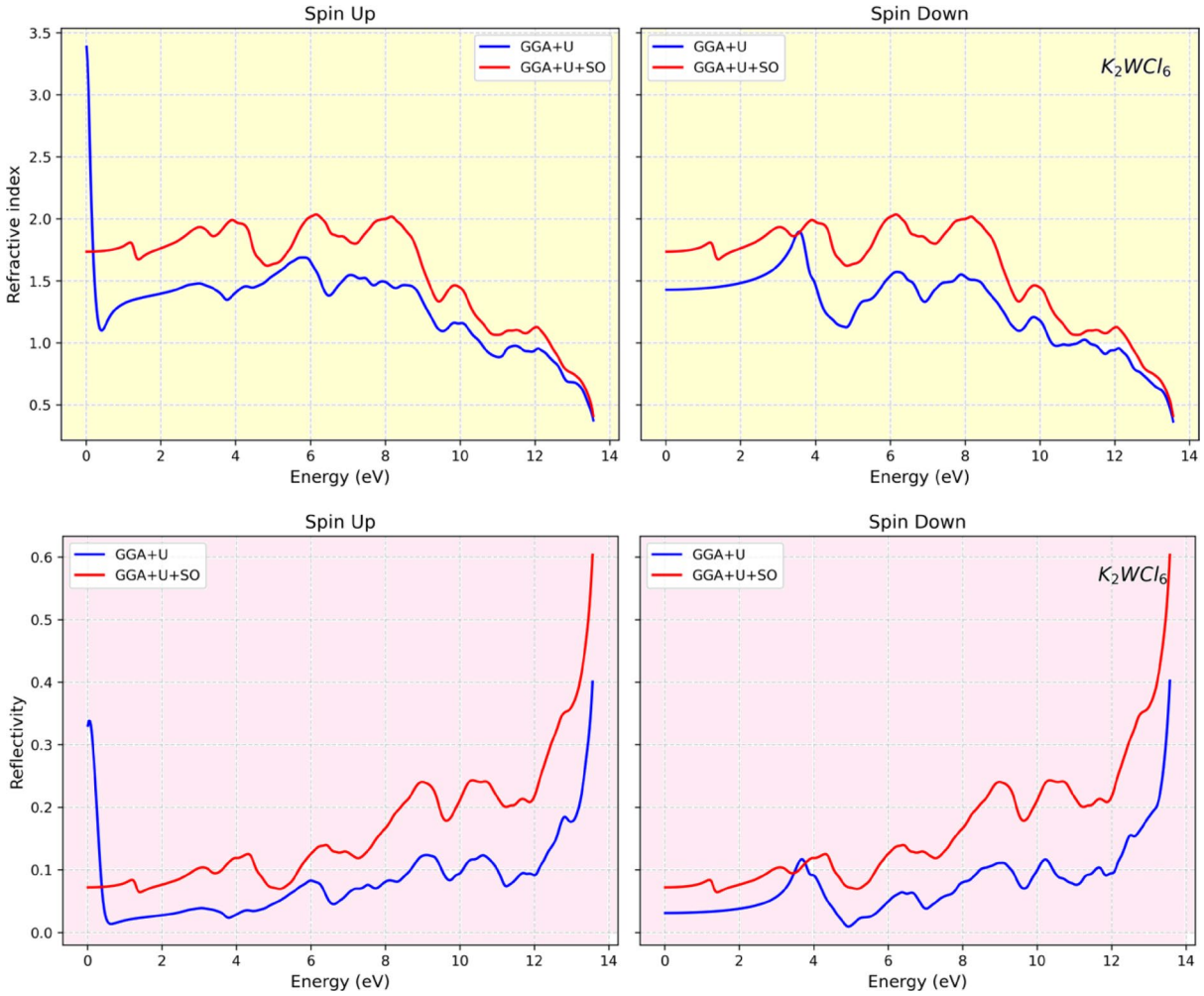


Fig. 8. Refractive index n(ω) (upper panel) and reflectivity R(ω) (lower panel) of K_2WCl_6 calculated using GGA + U and GGA + U+SOC.

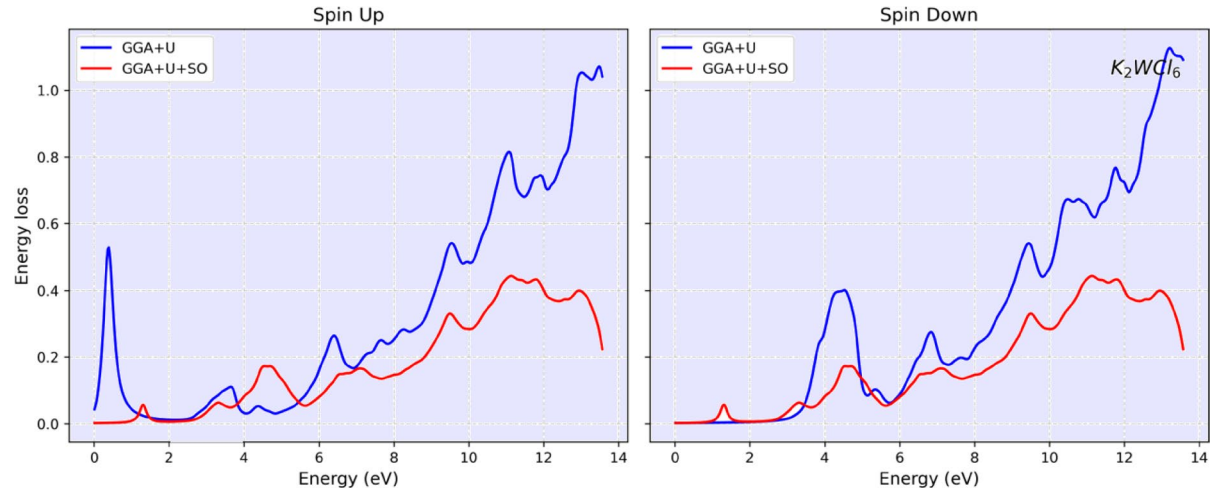


Fig. 9. Energy loss function L(ω) of K_2WCl_6 calculated using GGA + U and GGA + U+SOC.

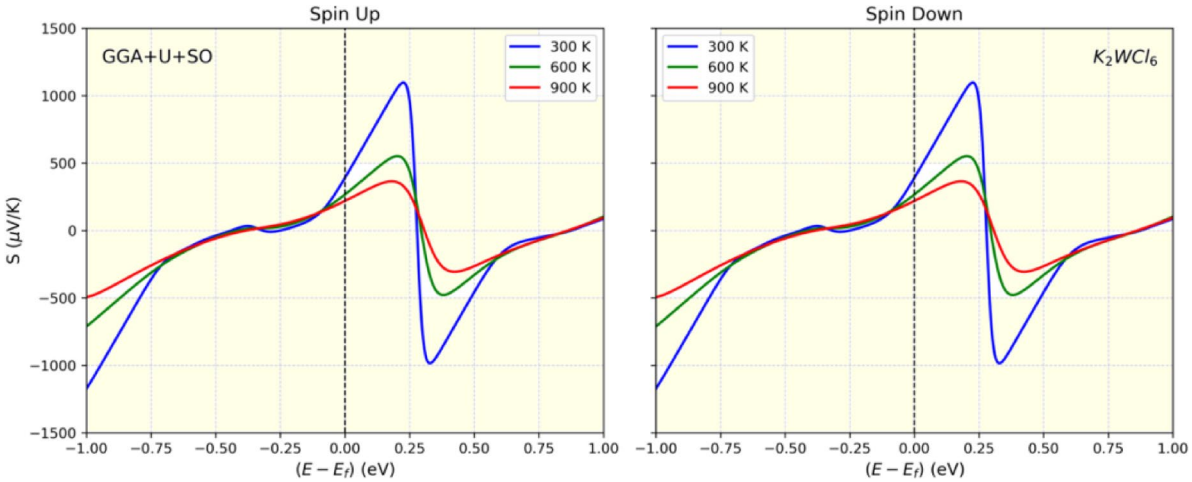


Fig. 10. Spin-resolved Seebeck coefficient S of K_2WCl_6 calculated using GGA + U+SOC.

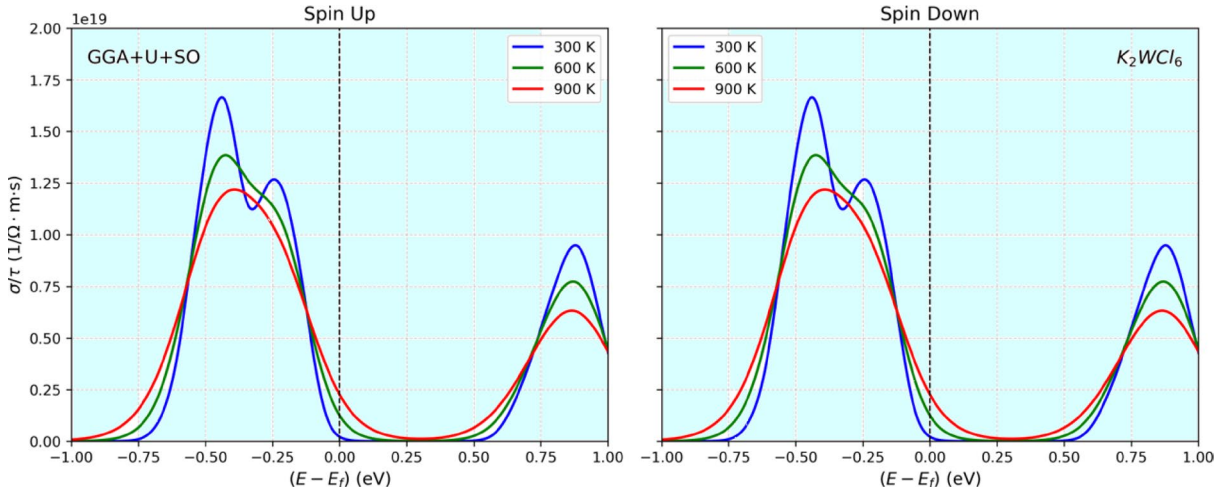


Fig. 11. Electrical conductivity per relaxation time (σ/τ) of K_2WCl_6 obtained within GGA + U+SOC.

conductivities. In real samples, electron–phonon, impurity, defect, grain-boundary, and spin-dependent scattering may produce a temperature- and energy-dependent relaxation time. A complete treatment would require deformation-potential theory or explicit electron–phonon scattering calculations, which are beyond the scope of the present study. Figure 10 shows the spin-dependent Seebeck coefficient as a function of $(E - E_F)$. The Seebeck coefficient displays large positive and negative values on either side of the Fermi level, reaching magnitudes of several hundred μV/K at optimal doping levels. The spin-up and spin-down channels exhibit distinct peak positions and magnitudes, reflecting their different electronic structures near the Fermi level[72]. At 300 K, the spin-down channel shows a particularly sharp peak below the Fermi level consistent with the remnant of the half-metallic gap edge. As temperature increases to 600 K and 900 K, thermal broadening reduces the peak values and shifts the optimal doping level, a typical behavior governed by the Mott relation[73]. More cautiously, the calculated results demonstrate a spin-dependent Seebeck response rather than the spin-Seebeck effect itself. A direct prediction of the spin-Seebeck effect would require an explicit treatment of thermally generated spin currents, magnon transport, spin-dependent scattering times, and interfacial spin-to-charge conversion. Accordingly, the present results are interpreted as evidence of spin-dependent thermoelectric transport.

The electrical conductivity per relaxation time σ/τ (Fig. 11) increases monotonically as the energy moves away from the Fermi level in both spin channels, reflecting the increasing density of transport-active states. The spin-up channel has a higher σ/τ due to its metallic character, while the spin-down channel shows a conductivity minimum near the band gap edge. The strong spin asymmetry in σ/τ implies a large spin polarization of the electrical conductivity, which is directly relevant for spin-filtering device concepts[74].

The electronic thermal conductivity per relaxation time κ_e/τ (Fig. 12) follows the Wiedemann-Franz relation qualitatively, increasing with the number of conducting channels. The spin-down channel shows a notable dip in κ_e/τ around the Fermi level at low temperatures, which could be exploited to achieve a large figure of merit $ZT = S^2\sigma T/\kappa$ in appropriately doped samples. The combination of large Seebeck coefficient, moderate electrical

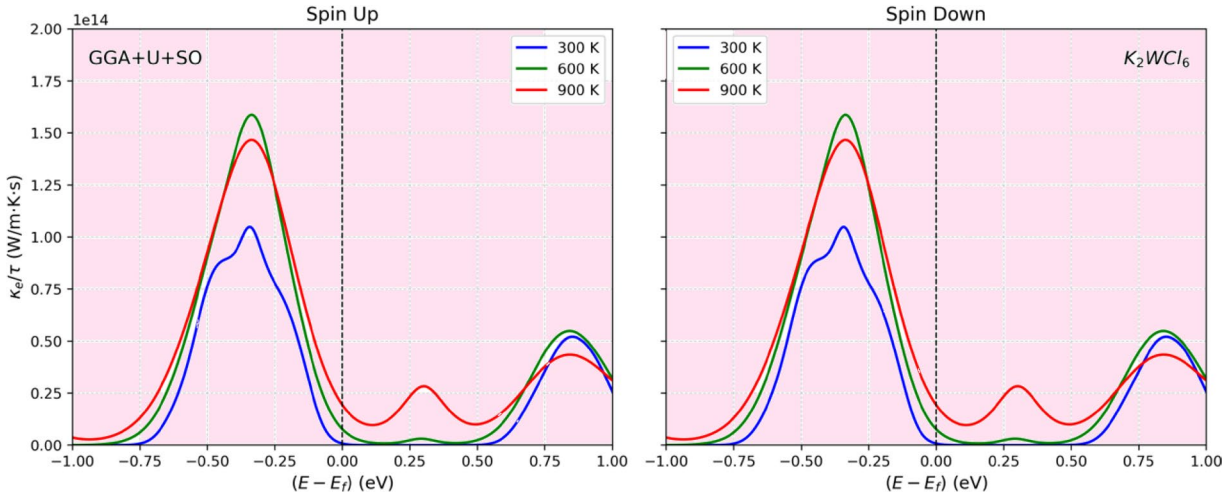


Fig. 12. Electronic thermal conductivity per relaxation time (κ_e/τ) of K_2WCl_6 obtained within GGA + U+SOC.

conductivity, and low thermal conductivity near the band edge in the spin-down channel suggests that n-type doped K_2WCl_6 is a promising candidate for spin-dependent thermoelectric energy conversion[75,76].

To estimate the absolute electrical and electronic thermal conductivities, a representative relaxation time of $\tau = 1 \times 10^{-14}$ s was adopted, so that $\sigma = (\sigma/\tau)\tau$ and $\kappa_e = (\kappa_e/\tau)\tau$. The lattice thermal conductivity κ_l was independently estimated using the Slack model[77]:

$$k_L = A\frac{\bar{M}\,\theta_D^3\,\delta}{\gamma^2 T n^{2/3}}$$

where M is the average atomic mass, $n = 9$ is the number of atoms per formula unit, δ is the cubic root of the volume per atom, and $\gamma = 2.043$ is the Grüneisen parameter obtained from the GIBBS analysis using the Slater approximation. The estimated κ_l values are approximately 2.363, 1.034, and 0.598 W m^{-1} K^{-1} at 300, 600, and 900 K, respectively. The strong decrease of κ_l with temperature reflects enhanced phonon scattering and thermal softening of the halide lattice. The total thermoelectric figure of merit was subsequently estimated using $ZT = (S^2\sigma T)/\kappa_{tot}$. At the intrinsic Fermi level, the estimated ZT values are approximately 0.016, 0.083, and 0.241 at 300, 600, and 900 K, respectively. The corresponding power factors are approximately 3.67×10^{-4}, 1.27×10^{-3}, and 3.12×10^{-3} W m^{-1} K^{-2}. These results indicate that the undoped material exhibits modest thermoelectric performance at room temperature, followed by a substantial improvement at elevated temperature. A search over the considered chemical-potential range reveals estimated maximum ZT values of approximately 0.367, 1.961, and 3.713 at 300, 600, and 900 K, respectively. The corresponding optimal chemical-potential shifts are approximately − 1.129, − 1.216, and + 0.353 eV relative to the intrinsic Fermi level. The negative shifts obtained at 300 and 600 K indicate that p-type carrier optimization is favorable in these temperature ranges, whereas the positive shift at 900 K suggests that an n-type regime may become advantageous at high temperature. The maximum calculated power factors are approximately 5.10×10^{-3}, 9.31×10^{-3}, and 1.084×10^{-2} W m^{-1} K^{-2} at 300, 600, and 900 K, respectively. The chemical potentials that maximize the power factor do not necessarily coincide with those that maximize ZT because the latter additionally depends on both electronic and lattice thermal conductivities.

The pronounced improvement obtained away from the intrinsic Fermi level indicates that carrier-concentration optimization may substantially enhance the thermoelectric response. Possible approaches include controlled electron or hole doping, aliovalent substitution, vacancy engineering, alloying, and nanostructuring. Carrier doping can shift the chemical potential toward favorable transport regions, whereas alloying and nanostructuring may further reduce κ_l through enhanced phonon scattering. Nevertheless, these modifications may also affect carrier mobility, magnetic ordering, structural stability, and the SOC-sensitive electronic phase. The reported ZT values should therefore be regarded as model-dependent theoretical estimates rather than definitive experimental predictions. In particular, the large optimal values are sensitive to the assumed constant relaxation time, the rigid-band approximation used to represent doping, and the Slack-model estimate of κ_l. More accurate quantitative predictions would require carrier-concentration-dependent scattering times, explicit defect calculations, and lattice thermal conductivity obtained from third-order interatomic force constants and the phonon Boltzmann transport equation.

The phonon dispersion curves and phonon density of states of K_2WCl_6 are presented in Fig. 13 along the high-symmetry directions of the cubic (W–L–Γ–X–Z–W). The unit cell of K_2WCl_6 contains 9 atoms (1 W, 2 K, 6Cl), giving rise to 27 phonon branches: 3 acoustic and 24 optical modes. The complete absence of imaginary (negative) phonon frequencies throughout the entire Brillouin zone unambiguously confirms the dynamic stability of K_2WCl_6 in its cubic Fm-3 m structure at zero temperature[78].

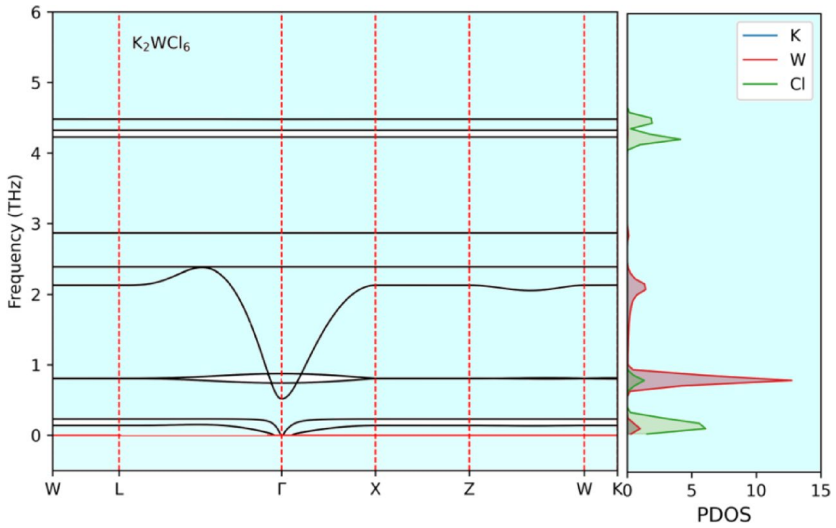


Fig. 13. Phonon dispersion curves (left) and phonon density of states (right) of K_2WCl_6 along the W–L–Γ–X–Z–W high-symmetry path. Contributions from K (blue), W (red), and Cl (green) atoms are shown in the PDOS panel.

A factor-group analysis was additionally performed to classify the zone-center vibrational modes. For the cubic Fm 3m structure, the complete vibrational representation at the Γ point can be written as.

$$\Gamma_{vib} = A_{1g} + E_g + 2T_{1g} + T_{2g} + 4T_{1u} + T_{2u}.$$

One of the T_{1u} representations corresponds to the triply degenerate acoustic modes. The optical representation is therefore.

$$\Gamma_{opt} = A_{1g} + E_g + T_{2g} + 3T_{1u} + 2T_{1g} + T_{2u}.$$

According to the selection rules of the centrosymmetric O_h point group, the A_{1g}, E_g, and T_{2g} modes are Raman-active, the three T_{1u} optical modes are infrared-active, and the $2T_{1g}$+T_{2u} modes are optically silent. The Raman- and infrared-active modes are mutually exclusive because the cubic structure possesses inversion symmetry. These symmetry assignments provide experimentally testable fingerprints for future Raman and infrared measurements of K_2WCl_6. The acoustic branches near the Γ point exhibit linear dispersion with slopes consistent with the acoustic velocities derived from the elastic constants (Sect. 3.2), providing an important internal consistency check between the elastic and phonon calculations[53]. The optical branches are grouped into two well-separated energy windows: a low-frequency manifold below ~5 THz dominated by K and Cl vibrations, and a higher-frequency group above ~7 THz associated primarily with W–Cl stretching modes within the WCl_6 octahedron. The low-frequency optical branches exhibit relatively weak dispersion and involve collective translations and distortions of the K sublattice and WCl_6 octahedra. Their low frequencies indicate a relatively soft lattice response and may provide effective phonon-scattering channels. This behavior is expected to suppress phonon group velocities and may contribute to a reduced lattice thermal conductivity, which is favorable for thermoelectric transport. The higher-frequency modes are more strongly associated with internal bending, breathing, and W–Cl stretching vibrations of the isolated WCl_6 octahedra. The phonon DOS on the right panel of Fig. 13 decomposes the total vibrational density into atomic contributions. Cl atoms contribute dominantly across the entire optical frequency range, while W contributes a sharp peak near the top of the spectrum corresponding to the breathing and stretching modes of the octahedron. K atoms have significant weight only in the low-frequency acoustic and lower optical branches, consistent with their role as charge-balancing spacers between the WCl_6 units[79,80]. The Debye temperature estimated from the phonon DOS ($\theta D \approx 292$ K) is in good agreement with the elastic-constant-based value (296.079 K), confirming the coherence of the computational methodology.

The predominance of Cl vibrations and the occurrence of several low-frequency optical branches suggest that lattice heat transport may be influenced by acoustic–optical phonon interactions. However, the harmonic phonon dispersion alone does not provide phonon lifetimes, linewidths, or three-phonon scattering rates. A quantitative evaluation of the intrinsic lattice thermal conductivity would require third-order interatomic force constants and a solution of the phonon Boltzmann transport equation. These anharmonic calculations were not performed in the present work. No experimental Raman or infrared spectra are currently used here to assign numerical frequencies for K_2WCl_6. Therefore, the present symmetry classification should be regarded as a theoretical prediction that can assist future experimental identification of the cubic phase. The explicit calculation of Raman intensities, Born effective charges, infrared oscillator strengths, and LO–TO splitting would require density-functional perturbation theory or finite-field calculations beyond the present frozen-phonon analysis. Halide double perovskites have recently attracted significant attention for thermoelectric

energy conversion owing to their favorable electronic structures and transport properties. Previous first-principles studies on compounds such as $(Cs_2,K_2,Rb_2)PbCl_6$, have reported positive Seebeck coefficients and promising thermoelectric responses, suggesting their suitability for energy harvesting devices[81]. Similarly, investigations on $(Cs_2,K_2,Rb_2)SnCl6$ revealed high Seebeck coefficients and significant power factors, indicating efficient carrier transport behavior in these halide systems. In addition, hybrid double perovskites such as $K_2(Sn, Se, Te)Br_6$ exhibit notable thermoelectric parameters with Seebeck coefficients exceeding 190 μV K^{-1} and figure-of-merit values approaching 0.8 at room temperature[82,83]. These results highlight the potential of halide double perovskites as promising materials for thermoelectric and renewable energy technologies.

The quasi-harmonic approximation accounts for the temperature dependence of the vibrational free energy through volume-dependent phonon frequencies but neglects explicit higher-order phonon–phonon interactions. This limitation is particularly relevant for relatively soft halide frameworks, in which anharmonic effects may become increasingly important at elevated temperatures. Therefore, the calculated thermodynamic quantities should be regarded as reliable within the harmonic and quasi-harmonic description, while their accuracy may gradually decrease in the upper part of the investigated temperature range. The Helmholtz free energy F(T) (Fig. 14) decreases monotonically with increasing temperature, as expected from thermodynamic principles ($F = U - TS$). The zero-point energy contribution, visible as the non-zero value of F at $T = 0$ K, amounts to approximately 0.35 eV/f.u., reflecting the zero-point quantum fluctuations of the light Cl atoms. The rate of decrease of F accelerates above ~200 K as more optical phonon modes become thermally populated. The relatively rapid thermal population of the optical modes is consistent with the moderate Debye temperature of K_2WCl_6 and indicates a comparatively soft vibrational framework. Such lattice softness can enhance phonon scattering and may contribute to a reduced lattice thermal conductivity, which is favorable for thermoelectric transport. However, an explicit evaluation of anharmonic free-energy contributions would require third- and higher-order interatomic force constants, which were not calculated in the present work.

The entropy S(T) (Fig. 15) rises continuously with temperature, starting from zero at absolute zero in accordance with the third law of thermodynamics. The rate of entropy increase is initially slow ($T < 100$ K, dominated by acoustic modes) and then accelerates as optical modes become active above the Debye temperature. At 300 K, $S \approx 110$ J mol^{-1} K^{-1}, and it continues to increase toward the classical limit at higher temperatures. The smooth and featureless entropy curve confirms the absence of any structural or magnetic phase transitions in this temperature range[84]. It should be emphasized that phonon-derived thermodynamic functions alone cannot establish the absence of a magnetic phase transition, because magnetic entropy and spin fluctuations are not included in the present vibrational free-energy calculation. Accordingly, the smooth behavior of S(T) confirms only that no phonon-related structural anomaly is predicted within the present approximation. The heat capacity at constant volume $C_v(T)$ (Fig. 16) exhibits the characteristic Debye-like T^3 dependence at low temperatures and converges toward the classical Dulong-Petit (DP) limit of $3nN_ak_B = 224.7$ J mol^{-1} K^{-1} (where $n = 9$ atoms per formula unit) at high temperatures[71]. At 300 K, $C_v \approx 180$ J mol^{-1} K^{-1}, which is already approximately 80% of the DP limit, consistent with the relatively low Debye temperature of 296 K. The rapid saturation of C_v above 300 K indicates that most vibrational degrees of freedom are already excited at room temperature, suggesting that the thermodynamic properties of K_2WCl_6 are largely classical at and above room temperature.

The relatively low Debye temperature further supports the description of K_2WCl_6 as a mechanically and vibrationally soft halide framework. From a practical perspective, this behavior may be beneficial for suppressing lattice heat transport, but it may also increase the sensitivity of the material to thermal expansion and anharmonic lattice distortions at elevated temperatures. Therefore, the predicted thermodynamic stability at high temperature should be interpreted with caution until explicit anharmonic calculations or experimental measurements become

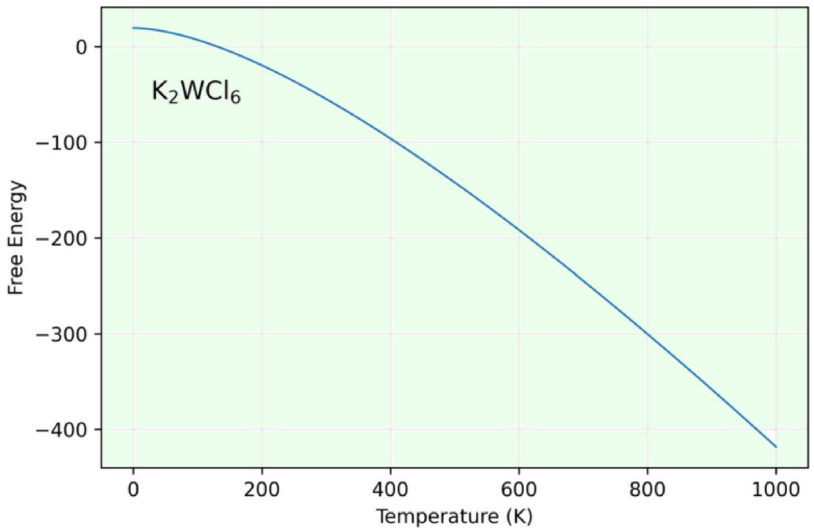


Fig. 14. Temperature dependence of the Helmholtz free energy F(T) of K_2WCl_6 calculated from phonon contributions within the quasi-harmonic approximation.

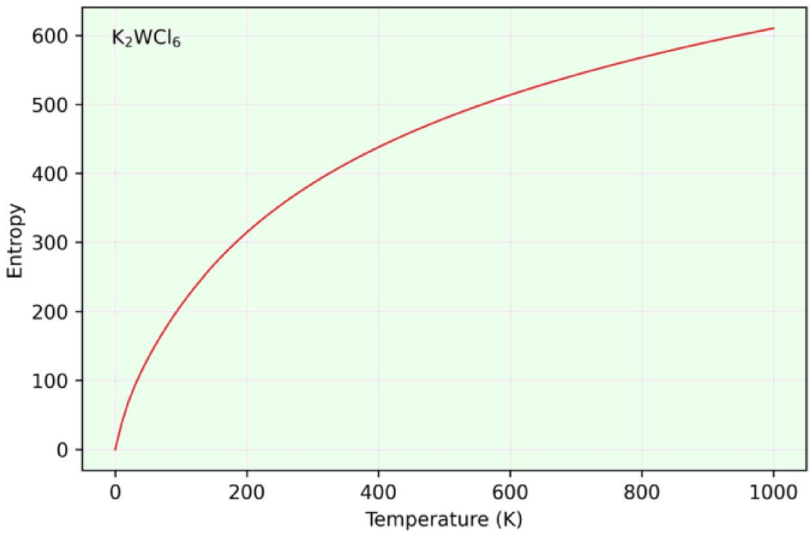


Fig. 15. Entropy S(T) of K_2WCl_6 as a function of temperature obtained from phonon calculations within the quasi-harmonic approximation.

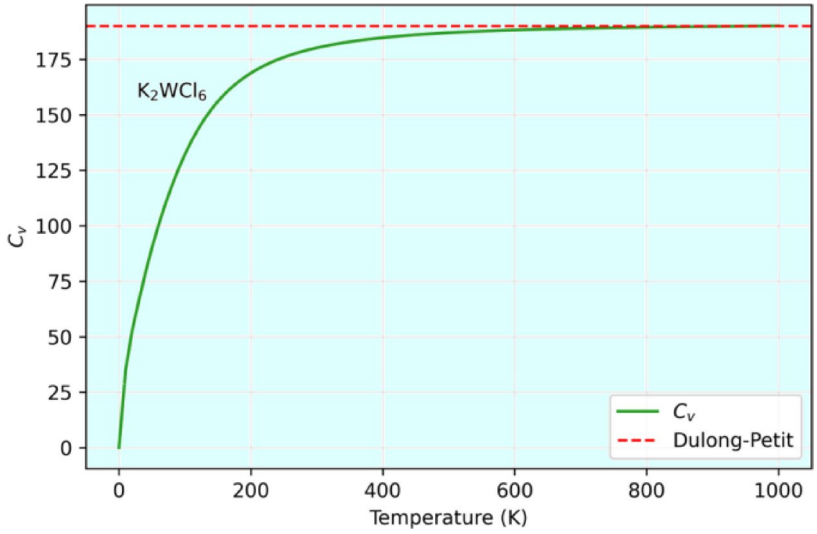


Fig. 16. Heat capacity at constant volume C_v(T) of K_2WCl_6 as a function of temperature. The red dashed line indicates the classical Dulong-Petit limit (224.7 J mol^{-1} K^{-1}).

available. The Grüneisen parameter and thermal expansion coefficient were explicitly evaluated using the GIBBS quasi-harmonic Debye analysis based on the calculated energy–volume data. The Grüneisen parameter is approximately 2.043, while the volumetric thermal expansion coefficient increases with temperature and reaches approximately 7.29×10^{-5} K^{-1} at 300 K and 8.69×10^{-5} K^{-1} at 1000 K. The corresponding equilibrium lattice parameter increases from 9.840 Å at 0 K to approximately 9.889 Å at 300 K and 10.076 Å at 1000 K, confirming progressive thermal expansion of the cubic lattice. Although the calculations were extended up to 1000 K to illustrate the overall thermodynamic trends, the quasi-harmonic Debye approximation is expected to be most reliable at low and moderate temperatures. At elevated temperatures, the decrease in the Debye temperature and bulk modulus, together with the increasing thermal expansion, indicates progressive lattice softening and enhanced anharmonic sensitivity. However, explicit higher-order phonon–phonon interactions, mode-resolved phonon lifetimes, thermal disorder, defect formation, and magnetic fluctuations are not captured by the present treatment. Therefore, the high-temperature results should be interpreted as quasi-harmonic estimates rather than a complete anharmonic description. Beyond intrinsic lattice thermodynamics, the operating stability of a real device can be strongly affected by defects, interfaces, carrier trapping, and temperature-dependent electrical transport. Defect-passivation strategies have recently been shown to suppress Fermi-level pinning and produce temperature-immune electrical operation in field-effect devices[64]. Although the underlying material and device architecture differ from K_2WCl_6, this result emphasizes that defect chemistry and thermal transport must be

considered when translating calculated bulk properties into device performance. Since defect formation energies, defect-assisted transport, surface degradation, and finite-temperature electrical stability were not evaluated here, the predicted functionality of K_2WCl_6 should be verified through defect calculations and temperature-dependent experimental measurements.

Conclusion

A comprehensive first-principles study of lead-free K_2WCl_6 was performed using FP-LAPW calculations within GGA + U and GGA + U+SOC. The compound is structurally, mechanically, and dynamically stable in the cubic Fm-3 m phase, with an optimized lattice parameter of 9.84 Å and a bulk modulus of 48.06 GPa. GGA + U predicts a robust half-metallic ferromagnetic ground state with a total magnetic moment of 2.00 μB/f.u., stable over U = 4–8 eV. Ferromagnetic ordering is energetically preferred over the AFM and NM configurations. Inclusion of SOC strongly modifies the W-t2g-derived states, yielding a magnetic-semiconducting solution within GGA + U+SOC, whereas TB-mBJ + SOC predicts a highly spin-polarized metallic state, highlighting the sensitivity of the relativistic electronic structure to the exchange-correlation treatment. K_2WCl_6 also exhibits strong ultraviolet optical absorption and marked spin-dependent optical and transport responses. Thermoelectric calculations predict increasing performance with temperature, with ZT reaching about 0.241 at 900 K at the intrinsic Fermi level and larger model-dependent values under optimized chemical potential. Phonon calculations show no imaginary modes, while the thermodynamic analysis indicates normal thermal expansion, lattice softening, and decreasing Debye temperature with increasing temperature. Overall, K_2WCl_6 emerges as a promising lead-free multifunctional material for spintronic, UV-optoelectronic, and high-temperature thermoelectric applications. Experimental synthesis and characterization are required to validate the predicted relativistic electronic phase and transport properties.

Data availability

Data availability statement: Data underlying the results presented in this paper are not publicly available at this time but may be obtained from the corresponding author upon reasonable request.

Received: 30 June 2026; Accepted: 31 August 2026
Published online: 12 September 2026

References

1. King, G. & Woodward, P. M. Cation Ordering in Perovskites. *J. Mater. Chem.* **20**, 5785–5796. https://doi.org/10.1039/B926757C (2010).
2. Vasala, S. & Karppinen, M. $A_2B'B''O_6$ Perovskites: A Review. Prog. *Solid State Chem.* **43**, 1–36. https://doi.org/10.1016/j.progsolidstchem.2014.08.001 (2015).
3. Kobayashi, K. I., Kimura, T., Sawada, H., Terakura, K. & Tokura, Y. Room-Temperature Magnetoresistance in an Oxide Material with an Ordered Double-Perovskite Structure. *Nature* **395**, 677–680. https://doi.org/10.1038/27167 (1998).
4. Serrate, D., De Teresa, J. M. & Ibarra, M. R. Double Perovskites with Ferromagnetism Above Room Temperature. *J. Phys. : Condens. Matter.* **19**, 023201. https://doi.org/10.1088/0953-8984/19/2/023201 (2007).
5. Zhao, X. G. et al. Cu–In Halide Perovskite Solar Cell Absorbers Enabling Grown by a Solution Route. *J. Am. Chem. Soc.* **139**, 6718–6725. https://doi.org/10.1021/jacs.7b02120 (2017).
6. Shi, Z. et al. Lead-Free Organic–Inorganic Hybrid Perovskites for Photovoltaic Applications: Recent Advances and Perspectives. *Adv. Mater.* **29**, 1605005. https://doi.org/10.1002/adma.201605005 (2017).
7. Kim, B. J. et al. Rotenberg. Novel Jeff = 1/2 Mott State Induced by Relativistic Spin-Orbit Coupling in Sr_2IrO_4. *Phys. Rev. Lett.* **101**, 076402. https://doi.org/10.1103/PhysRevLett.101.076402 (2008).
8. Witczak-Krempa, W., Chen, G., Kim, Y. B. & Balents, L. Correlated Quantum Phenomena in the Strong Spin-Orbit Regime. *Annu. Rev. Condens. Matter Phys.* **5**, 57–82. https://doi.org/10.1146/annurev-conmatphys-020911-125138 (2014).
9. Reuter, K., Scheffler, M. & Composition Structure, and Stability of RuO_2(110) as a Function of Oxygen Pressure. *Phys. Rev. B.* **65**, 035406. https://doi.org/10.1103/PhysRevB.65.035406 (2001).
10. Morss, L. R., Siegal, M., Stenger, L. & Edelstein, N. Preparation of Cubic Chloro Complex Compounds of Trivalent Metals. *Inorg. Chem.* **9**, 1771–1775. https://doi.org/10.1021/ic50089a034 (1970).
11. Nganba Meetei, O., Erten, O., Mukherjee, A., Randeria, M. & Trivedi, N. Woodward. Theory of Half-Metallic Double Perovskites. I. Double Exchange Mechanism. *Phys. Rev. B.* **87**, 165104. https://doi.org/10.1103/PhysRevB.87.165104 (2013).
12. Hamada, N. Electronic Structure of Double Perovskites. *J. Phys. Chem. Solids.* **54**, 1195 (1993).
13. Anisimov, V. I., Zaanen, J. & Andersen, O. K. Band Theory and Mott Insulators: Hubbard U Instead of Stoner I. *Phys. Rev. B.* **44**, 943–954. https://doi.org/10.1103/PhysRevB.44.943 (1991).
14. Dudarev, S. L., Botton, G. A., Savrasov, S. Y., Humphreys, C. J. & Sutton, A. P. Electron-Energy-Loss Spectra and the Structural Stability of Nickel Oxide: An LSDA + U Study. *Phys. Rev. B.* **57**, 1505–1509. https://doi.org/10.1103/PhysRevB.57.1505 (1998).
15. Shick, A. B., Liechtenstein, A. I. & Pickett, W. E. Implementation of the LDA + U Method Using the Full-Potential Linearized Augmented Plane-Wave Basis. *Phys. Rev. B.* **60**, 10763. https://doi.org/10.1103/PhysRevB.60.10763 (1999).
16. Novák, P., Kuneš, J., Chaput, L. & Pickett, W. E. Exact Exchange for Correlated Electrons. *Phys. Status Solidi B.* **243**, 563–572. https://doi.org/10.1002/pssb.200541371 (2006).
17. Navas, J. et al. New Insights into Organic–Inorganic Hybrid Perovskite $CH_3NH_3PbI_3$ Nanoparticles. *Nanoscale* **7**, 6216–6229. https://doi.org/10.1039/C5NR00041F (2015).
18. Filip, M. R., Liu, X., Miglio, A., Hautier, G. & Giustino, F. Phase Diagrams and Stability of Lead-Free Halide Double Perovskites. *J. Phys. Chem. C.* **122**, 158–170. https://doi.org/10.1021/acs.jpcc.7b10370 (2018).
19. Baranowski, M. & Plochocka, P. Excitons in Metal-Halide Perovskites. *Adv. Energy Mater.* **10**, 1903659. https://doi.org/10.1002/aenm.201903659 (2020).
20. Saini, H. S., Singh, M., Reshak, A. H. & Kashyap, M. K. Variation of Half-Metallicity and Magnetism in K_2OsX_6 (X = F, Cl, Br, I) Double Perovskites. *J. Magn. Magn. Mater.* **331**, 1–6 (2013).
21. Ahmad, S. & Mukherjee, S. A. Comparative Study of Electronic Properties of Bulk MoS_2 and Its Monolayer Using DFT Technique: Application of Mechanical Strain on MoS_2 Monolayer. *Graphene* **3**, 52–59. https://doi.org/10.4236/graphene.2014.34008 (2014).
22. Hussain, A., Ullah, S. & Farhan, M. A. Fine Tuning the Optoelectronics and Magnetic Properties of K_2MoCl_6 Via GGA + U. *RSC Adv.* **6**, 55509–55517 (2016).

23. Batouche, M. et al. First-principles investigation of half-metallic vacancy-ordered double perovskites K_2MBr_6 (M = Re, W, Ru, Os) for visible-light photocatalytic hydrogen production and CO_2 reduction. *Polyhedron* **296**, 118213. https://doi.org/10.1016/j.poly.2026.118213 (2026).
24. Wang, J. et al. Pressure modulates emission of Cs_2WCl_6 in the NIR-II window. *Laser Photonics Rev.* **19**, e01238. https://doi.org/10.1002/lpor.202501238 (2025).
25. Elkenany, E. B. et al. Electronic, magnetic, optical, and thermoelectric properties of K_2OsCl_6 for spintronic and energy harvesting applications. *Sci. Rep.* **16**, 16465. https://doi.org/10.1038/s41598-026-44862-1 (2026).
26. El Goutni, M. E. A., Batouche, M., Ferjani, H. & Seddik, T. Optoelectronic properties of spin–orbit coupled alkali-metal double perovskites for renewable hydrogen and CO_2 conversion. *J. Supercond. Novel Magn.* **38**, 254. https://doi.org/10.1007/s10948-025-07097-1 (2025).
27. Fatmi, M., Ghebouli, M. A., Bouferrache, K., Ghebouli, B. & Alomairy, S. Mustafa Jaipallah Abdelmageed Abualreish, Aseel Smerat & Murat Yaylacı, Structural, electronic, optical, and thermoelectric properties of $CaXO_3$ (X = Si, Ge, Ti) perovskite for photovoltaics and optical devices. *Sci. Rep.* **15**, 43569. https://doi.org/10.1038/s41598-025-31002-4 (2025).
28. Bouferrache, K. et al. Crystal structure, mechanical, electronic, optical and thermoelectric characteristics of Cs_2MCl_6 (M = Se, Sn, Te and Ti) cubic double perovskites. *Results Phys.* **56**, 107138. https://doi.org/10.1016/j.rinp.2023.107138 (2024).
29. Zada, Z. et al. Electronic band profiles, magnetic stability, antiferromagnetic spins ordering and thermodynamics properties of novel antiferromagnet $CaCr_2Sb_2$. *Eur. Phys. J. Plus*. **136**, 371. https://doi.org/10.1140/epjp/s13360-021-01356-5 (2021).
30. Ullah, H. & Khalid, S. Exchange interactions, half metallic ferromagnetism, mechanical, thermal and magneto-electronic properties of full Heusler alloys Co_2YGe (Y = Mn, Fe) for acoustical and spintronic devices. *Phys. B: Condens. Matter*. **615**, 413060. https://doi.org/10.1016/j.physb.2021.413060 (2021).
31. Manzar, A., Murtaza, G., Khenata, R., Muhammad, S. & Hayatullah Electronic band structure and optical response of spinel SnX_2O_4 (X = Mg, Zn) through modified Becke–Johnson potential. *Chin. Phys. Lett.* **30**, 047401. https://doi.org/10.1088/0256-307X/30/4/047401 (2013).
32. Ali, L. et al. First-principles study on the electronic band profiles, structural, mechanical and thermoelectric properties of semiconducting $MgSc_2Te_4$ and MgY_2Te_4 spinels. *Eur. Phys. J. Plus*. **137**, 377. https://doi.org/10.1140/epjp/s13360-022-02547-4 (2022).
33. Yasin, S., Ullah, H., Abualnaja, K. M. & Murtaza, G. Structural stability, half-metallic ferromagnetism, magneto-optical, and thermoelectric properties of europium-based ternary Zintl compounds $EuZn_2C_2$ (C = P, As): A promising alternative for spintronics and thermoelectric applications. *J. Inorg. Organomet. Polym. Mater.* **35**, 6739–6760. https://doi.org/10.1007/s10904-025-03692-w (2025).
34. Yasin, S. et al. Magnetism, optoelectronic, and thermoelectric properties of $RELi_2X_2$ (RE = Ce, Pr; X = P, As) rare-earth Zintl semiconductors for optoelectronic and waste-heat-recovery applications. *Opt. Quantum Electron.* **58**, 184. https://doi.org/10.1007/s11082-026-08757-9 (2026).
35. Yasin, S., Ullah, H., AbdelAll, N., Jaouadi, M. & Murtaza, G. Discovery of high-performance multifunctional Zintl compounds: Ab initio investigation of UCu_2P_2 and UCu_2As_2 for thermoelectric and optoelectronic applications. *Adv. Theory Simul.* **9**, e70412. https://doi.org/10.1002/adts.70412 (2026).
36. Blaha, P. et al. WIEN2k: An APW + lo Program for Calculating the Properties of Solids. *J. Chem. Phys.* **152**, 074101. https://doi.org/10.1063/1.5143061 (2020).
37. Singh, D. J., Nordstrom, L. & Planewaves *Pseudopotentials, and the LAPW Method* 2nd edn (Springer, 2006). https://doi.org/10.1007/978-0-387-29684-5
38. Cottenier, S. *Density Functional Theory and the Family of (L)APW-Methods: A Step-by-Step Introduction; Instituutvoor Kern-enStralingsfysica* (Belgium, 2002).
39. Perdew, J. P., Burke, K. & Ernzerhof, M. Generalized Gradient Approximation Made Simple. *Phys. Rev. Lett.* **77**, 3865–3868. https://doi.org/10.1103/PhysRevLett.77.3865 (1996).
40. Liechtenstein, A. I., Anisimov, V. I. & Zaanen, J. Density-Functional Theory and Strong Interactions: Orbital Ordering in Mott-Hubbard Insulators. *Phys. Rev. B*. **52**, R5467–R5470. https://doi.org/10.1103/PhysRevB.52.R5467 (1995).
41. Kuneš, J., Novák, P., Schmid, R., Blaha, P. & Schwarz, K. Electronic Structure of fcc Th: Spin-Orbit Calculation with 6p1/2 Local Orbital Extension. *Phys. Rev. B*. **64**, 153102. https://doi.org/10.1103/PhysRevB.64.153102 (2001).
42. Blaha, P., Schwarz, K., Sorantin, P., Trickey, S. B. & Full-Potential Linearized Augmented Plane Wave Programs for Crystalline Systems. *Comput. Phys. Commun.* **59**, 399–415. https://doi.org/10.1016/0010-4655(90)90187-6 (1990).
43. Monkhorst, H. J. & Pack, J. D. Special Points for Brillouin-Zone Integrations. *Phys. Rev. B*. **13**, 5188–5192. https://doi.org/10.1103/PhysRevB.13.5188 (1976).
44. Murnaghan, F. D. The Compressibility of Media Under Extreme Pressures. *Proc. Natl. Acad. Sci. USA*. **30**, 244–247. https://doi.org/10.1073/pnas.30.9.244 (1944).
45. Voigt, W. *Lehrbuch der Kristallphysik* (Leipzig, 1928).
46. Reuss, A. Berechnung der Fließgrenze von Mischkristallen. *Z. Angew Math. Mech.* **9**, 49–58. https://doi.org/10.1002/zamm.19290090104 (1929).
47. Born, M. & Huang, K. *Dynamical Theory of Crystal Lattices* (Oxford University Press, 1954).
48. Mouhat, F. & Coudert, F. X. Necessary and Sufficient Elastic Stability Conditions in Various Crystal Systems. *Phys. Rev. B*. **90**, 224104. https://doi.org/10.1103/PhysRevB.90.224104 (2014).
49. Ambrosch-Draxl, C. & Sofo, J. O. Linear Optical Properties of Solids Within the Full-Potential Linearized Augmented Planewave Method. *Comput. Phys. Commun.* **175**, 1–14. https://doi.org/10.1016/j.cpc.2006.03.005 (2006).
50. Wooten, F. *Optical Properties of Solids* (Academic, 1972). https://doi.org/10.1016/C2013-0-07656-6
51. Fox, M. *Optical Properties of Solids* 2nd edn (Oxford University Press, 2010).
52. Madsen, G. K. H. & Singh, D. J. BoltzTraP. A Code for Calculating Band-Structure Dependent Quantities. *Comput. Phys. Commun.* **175**, 67–71. https://doi.org/10.1016/j.cpc.2006.03.007 (2006).
53. Togo, A. & Tanaka, I. First Principles Phonon Calculations in Materials Science. *Scr. Mater.* **108**, 1–5. https://doi.org/10.1016/j.scriptamat.2015.07.021 (2015).
54. Chaput, L., Togo, A., Tanaka, I. & Hug, G. Phonon-Phonon Interactions in Transition Metals. *Phys. Rev. B*. **84**, 094302. https://doi.org/10.1103/PhysRevB.84.094302 (2011).
55. Baroni, S., de Gironcoli, S., Dal Corso, A. & Giannozzi, P. Phonons and Related Crystal Properties from Density-Functional Perturbation Theory. *Rev. Mod. Phys.* **73**, 515–562. https://doi.org/10.1103/RevModPhys.73.515 (2001).
56. Parlinski, K., Li, Z. Q. & Kawazoe, Y. First-Principles Determination of the Soft Mode in Cubic ZrO_2. *Phys. Rev. Lett.* **78**, 4063–4066. https://doi.org/10.1103/PhysRevLett.78.4063 (1997).
57. Xu, W. & Zheng, Y. Q. Crystal structure of dipotassium hexachlorotungstate(IV), $K_2[WCl_6]$, Zeitschrift für Kristallographie – New Crystal Structures, vol. 220, no. 3, p. 323, (2005). https://doi.org/10.1524/ncrs.2005.220.3.323
58. Haines, J., Léger, J. M. & Bocquillon, G. Synthesis and Design of Superhard Materials. *Annu. Rev. Mater. Res.* **31**, 1–23. https://doi.org/10.1146/annurev.matsci.31.1.1 (2001).
59. Pugh, S. F. Relations Between the Elastic Moduli and the Plastic Properties of Polycrystalline Pure Metals. *Philos. Mag.* **45**, 823–843. https://doi.org/10.1080/14786440808520496 (1954).
60. de Groot, R. A., Mueller, F. M., van Engen, P. G. & Buschow, K. H. J. New Class of Materials: Half-Metallic Ferromagnets. *Phys. Rev. Lett.* **50**, 2024–2027. https://doi.org/10.1103/PhysRevLett.50.2024 (1983).

61. Pickett, W. E., Moodera, J. S. & Half *Metallic Magnets Phys. Today* **54**, 39–44. https://doi.org/10.1063/1.1381101 (2001).
62. Žutić, I., Fabian, J., Das Sarma, S. & Spintronics Fundamentals and Applications. *Rev. Mod. Phys.* **76**, 323–410. https://doi.org/10.1103/RevModPhys.76.323 (2004).
63. Zheng, Z. et al. Chen. All-Electrical Perpendicular Switching of Chiral Antiferromagnetic Order. *Nat. Mater.* **24**, 1407–1413. https://doi.org/10.1038/s41563-025-02228-4 (2025).
64. Qi, J. et al. Achieving zero-temperature coefficient point behavior by defect passivation for temperature-immune organic field-effect transistors. *Adv. Mater.* **36**, 2400089. https://doi.org/10.1002/adma.202400089 (2024).
65. Ehrenreich, H. & Philipp, H. R. Optical Properties of Ag and Cu. *Phys. Rev.* **128**, 1622–1629. https://doi.org/10.1103/PhysRev.128.1622 (1962).
66. Dressel, M. & Grüner, G. *Electrodynamics of Solids* (Cambridge University Press, 2002). https://doi.org/10.1017/CBO9780511606168
67. Wemple, S. H. & DiDomenico, M. Behavior of the Electronic Dielectric Constant in Covalent and Ionic Materials. *Phys. Rev. B.* **3**, 1338–1351. https://doi.org/10.1103/PhysRevB.3.1338 (1971).
68. Penn, D. R. Wave-Number-Dependent Dielectric Function of Semiconductors. *Phys. Rev.* **128**, 2093–2097. https://doi.org/10.1103/PhysRev.128.2093 (1962).
69. Ritchie, R. H. Plasma Losses by Fast Electrons in Thin Films. *Phys. Rev.* **106**, 874–881. https://doi.org/10.1103/PhysRev.106.874 (1957).
70. Li, J. et al. Highly efficient pure red light-emitting diodes enabled by multifunctional ligand-coordinated $CsPbI_3$ quantum dots. *Nano Energy*. **140**, 111055. https://doi.org/10.1016/j.nanoen.2025.111055 (2025).
71. Kittel, C. *Introduction to Solid State Physics* 8th edn (Wiley, 2005).
72. Rowe, D. M. *CRC Handbook of Thermoelectrics* (CRC, 1995). https://doi.org/10.1201/9781420049718
73. Mott, N. F. Electrons in Disordered Structures. *Adv. Phys.* **16**, 49–144. https://doi.org/10.1080/00018736700101265 (1967).
74. Bauer, G. E. W., Saitoh, E. & van Wees, B. J. Spin Caloritronics. *Nat. Mater.* **11**, 391–399. https://doi.org/10.1038/nmat3301 (2012).
75. Snyder, G. J., Toberer, E. S. & Complex *Thermoelectric Mater. Nat. Mater.* **7**, 105–114. https://doi.org/10.1038/nmat2090 (2008).
76. Goldsmid, H. J. *Introduction to Thermoelectricity* (Springer, 2010). https://doi.org/10.1007/978-3-642-00716-3
77. Ameur, R. et al. Half-Metallicity and Spin-Gapless Semiconducting Properties in FeCrTiM (M = Al, As, Si) Quaternary Heusler Alloys for Spintronic, Thermoelectric and Optoelectronic Applications. *Adv. Compos. Hybrid. Mater.* **8**, 366. https://doi.org/10.1007/s42114-025-01466-z (2025).
78. Dove, M. T. *Introduction to Lattice Dynamics* (Cambridge University Press, 1993). https://doi.org/10.1017/CBO9780511619885
79. Bilz, H. & Kress, W. *Phonon Dispersion Relations in Insulators* (Springer, 1979). https://doi.org/10.1007/978-3-642-81347-4
80. Brüesch, P. *Phonons: Theory and Experiments I* (Springer, 1982). https://doi.org/10.1007/978-3-642-81781-6
81. Ghebouli, M. A., Bouferrache, K., Alanazi, F. K., Ghebouli, B. & Fatmi, M. Computational Insights into the Stability, Mechanical, Optoelectronic, and Thermoelectric Characteristics Investigation on Lead-Based Double Perovskites of $(Cs_2, K_2, Rb_2)PbCl_6$: Promising Candidates for Optoelectronic Applications. *Adv. Theory Simul.* **8**, 2400938. https://doi.org/10.1002/adts.202400938 (2025).
82. Ghebouli, M. A. et al. Mechanical, Optoelectronic and Thermoelectric Behaviors of Inorganic Metal Halide Double Perovskites $(Cs_2, K_2, Rb_2)SnCl_6$: Promising Green Energy Alternatives. *Solid State Commun.* **397**, 115831. https://doi.org/10.1016/j.ssc.2025.115831 (2025).
83. Bouferrache, K., Ghebouli, M. A., Ghebouli, B., Fatmi, M. & Ahmed, S. I. Organic–Inorganic Hexahalometalate-Crystal Semiconductor $K_2(Sn, Se, Te)Br_6$ Hybrid Double Perovskites for Solar Energy Applications. *RSC Adv.* **15**, 11923–11933. https://doi.org/10.1039/D5RA00862J (2025).
84. Wallace, D. C. *Thermodynamics of Crystals* (Wiley, 1972).

Acknowledgements

The authors are thankful to the Deanship of Graduate Studies and Scientific Research at Najran University for funding this work under the Elite Funding Program grant code (NU/EP/SERC/14/4230-1).

Author contributions

Conceptualization: K. Bouferrache, Murat YaylacıData curation: M.A. Ghebouli, M. Abdelgaber, Elkenany Brens ElkenanyFormal analysis: Aseel Smerat, R. Dhahri, A. M. AbdelghanyValidation: M. Fatmi,

Funding

Not applicable.

Declarations

Competing interests

The authors declare no competing interests.

Additional information

Correspondence and requests for materials should be addressed to M.A.

Reprints and permissions information is available at www.nature.com/reprints.

Publisher's note Springer Nature remains neutral with regard to jurisdictional claims in published maps and institutional affiliations.

Open Access This article is licensed under a Creative Commons Attribution-NonCommercial-NoDerivatives 4.0 International License, which permits any non-commercial use, sharing, distribution and reproduction in any medium or format, as long as you give appropriate credit to the original author(s) and the source, provide a link to the Creative Commons licence, and indicate if you modified the licensed material. You do not have permission under this licence to share adapted material derived from this article or parts of it. The images or other third party material in this article are included in the article's Creative Commons licence, unless indicated otherwise in a credit line to the material. If material is not included in the article's Creative Commons licence and your intended use is not permitted by statutory regulation or exceeds the permitted use, you will need to obtain permission directly from the copyright holder. To view a copy of this licence, visit http://creativecommons.org/licenses/by-nc-nd/4.0/.

© The Author(s) 2026, modified publication 2026